Elastic Light Scattering, Fluorescence, and Raman Spectroscopy of a Diamond Microsphere

by

Mustafa Mert Bayer

A Dissertation Submitted to the

Graduate School of Sciences and Engineering

in Partial Fulfillment of the Requirements for the Degree of

Master of Science

in

Optoelectronics and Photonics Engineering

KOÇ UNIVERSITY

August 21, 2017

MSc Thesis

Koç University

Koç University Graduate School of Sciences and Engineering

This is to certify that I have examined this copy of a master's thesis by

Mustafa Mert Bayer

and have found that it is complete and satisfactory in all respects, and that any and all revisions required by the final examining committee have been made.

Committee Members:

_____

Prof. Ali SERPENGÜZEL

_____

Prof. Alper KİRAZ

_____

Asst. Prof. Onur FERHANOĞLU

Date: _____

ABSTRACT

Over the past decades, morphology dependent resonances, the optical resonances occurring by the interaction of light with microspheres of various materials, were vastly investigated. Spherical microcavities have diverse applications due to their high concentration of modes in small volumes at optical frequencies and high Q-factors. The localization of the electromagnetic waves inside the microsphere is realized by total internal reflection. Microspheres provide the concave surface for light to circumnavigate around the microcavity, giving rise to whispering gallery modes.

Because of its unique lattice structure, robust physical properties, as well as its distinctive optical properties, different forms of diamond were vastly investigated for various applications. As is well known, nitrogen vacancy (NV) centers inside the diamond lattice give rise to such applications by replacing two carbon atoms by one nitrogen atom and a vacancy, that yields a floating electron at the NV^- center.

In this thesis, Raman and photoluminescence spectroscopy is performed with various diamond samples including a diamond microsphere. The measurement setup is presented for both spectroscopies. NV centers exhibit 575 nm or 637 nm zero phonon lines along with their corresponding phonon side bands depending on the charge state of the point defect, NV^0 and NV^-, respectively. A 572 nm inelastic Raman scattering (1332.25 cm^{-1}) is observed with 532 nm excitation laser due to the vibrational state of carbon-carbon bonds with sp^3 configuration, whereas sp^2 hybridization (1444.56 cm^{-1}) yields inelastically scattered photons with 576 nm wavelength. It is possible to identify the main impurities within the diamond lattice, and confirm the carbon-carbon bonds with spectroscopic techniques.

In addition, the demonstration of a diamond microsphere whispering gallery modes resonator in the standard telecom wavelengths between 1426.10 nm and 1427.42 nm in the 90° elastic light scattering for both transverse magnetic and transverse electric

polarizations is realized. The highest measured whispering gallery mode Q-factor is on the order of 10^4, and the mode spacing 0.332 nm for both transverse polarizations. The coupling of the continuous wave tunable infrared excitation laser to the diamond microsphere is achieved by a single mode silica optical fiber half coupler.

All in all, diamond is a unique material with particular optical properties. Utilizing such properties in a spherical morphology can give rise to distinctive applications. It is essential to observe the aspects of the whispering gallery modes created by the light circumnavigating a diamond microsphere such as mode spacing and Q-factor to classify the properties of a 1 mm synthetically grown spherical diamond microresonator. Such a diamond resonator can further be used as stable optical frequency comb generators or lasing microcavities by exploiting the nitrogen vacancy centers present within the lattice of the diamond.

ÖZET

Geçtiğimiz yıllarda ışık ve çeşitli gereçlerden üretilmiş mikroyuvarlar arasındaki etkileşim, yapıya bağlı optik çınlamalar (MDR) olarak adlandırılmış ve incelenmiştir. Mikroçınlaçlar, yüksek nitelik katsayıları (Q-factor) ve dar optik sıklık bantlarına yüksek sayıda ışık kipi sığdırmalarından ötürü çeşitli uygulamalarda kullanılmışlardır. Elektromanyetik dalgaların mikroyuvarlarda yerelleşmesi tam iç yansımayla (TIR) gerçekleşir. Bu mikroyuvarlar ışığın yuvar çevresinde dönmesini, içbükey yüzeyleri ile gerçekleştirerek, fısıldayan geçit kiplerinin (WGM) oluşmasını sağlarlar.

Değişik atom örgüsü, güçlü fiziksel özellikleri ve çeşitlilik yaratan optik özelliklerinden dolayı, çeşitli elmas örnekler çeşitli uygulamalarda kullanılmak üzere incelenmiştir. Bilindiği gibi, elmas örgüsünün içine yerleşmiş azot boşluk özekleri (NV), yan yana bulunan iki kömür atomunu elmas örgüsünden çıkartarak oluşurlar, böylece NV^- özeğinde bir fazla elektron bulunur.

Bu tezde, çeşitli elmas örnekler ve bir elmas mikroyuvar ile Raman ve fotoışıma izgeölçümleri yapılmıştır. İki tür izgeölçümü için kullanılan deney düzenekleri sunulmuştur. NV^0 ve NV^- özeklerinden 575 nm ve 637 nm olmak üzere, iki sıfır fonon çizgisi ışıması ile bunları izleyen fonon yanbant ışımaları gözlemlenmiştir. 532 nm lazer kaynağı kullanılarak gözlemlenen Raman saçılmasından ise 572 nm (1332.25 cm^{-1}) de esnek olmayan saçılma görülmüştür. Bu Raman kayması sp^3 düzeninde bağ yapan C-C atomlarınca oluşur. sp^2 düzenindeki C-C bağları ise 576 nm'de Raman kayması (1444.56 cm^{-1}) yapar. Fotoışıma izgeölçümü kullanılarak elmas içindeki safsızlık, elmasın türü ve C-C bağlarının durumu bulunabilir.

Elmas mikroyuvardan 90º'de esnek saçılma yapan WGM çınlaması kızılaltı uzakiletim (Telekom) dalgaboyu olan 1426,1 - 1427,42 nm arasında enine elektrik (TE) ve enine manyetik (TM) kutuplu bir lazerle ölçülmüştür. Gözlemlenen en yüksek nitelik katsayısı Q-factor 10^4 ve ölçülen kip aralığı 0,332 nm'dir. Dalgaboyu değiştirilebilen

sürekli uyarma lazeri ile elmas küre arasındaki bağlaşma, bir optik lif yarı bağlaştırıcıyla (OFHC) gerçekleştirilir.

Sonuçta, elmas kendisine özgü optik özelliklerinden dolayı eşi benzeri olmayan değerli bir taştır. Bu eşsiz özellikleri küre yapısında kullanmak farklı uygulamalara yol açabilir. Bu bağlamda, 1 mm çapındaki elmas mikroyuvarının etrafında dönen ışık yardımıyla oluşan fısıldayan geçit kiplerinin, kip aralığı ve nitelik faktörü gibi özelliklerinin incelenmesi büyük bir önem taşır. Böyle bir elmas mikroçınlaç optik sıklık tarağı üreticisi veya NV lazer mikroçınlacı olarak kullanılabilir.

ACKNOWLEDGEMENTS

First and foremost, I would like to express my special thanks of gratitude to my academic advisor and mentor Prof. Ali Serpengüzel for giving me the chance to work in Koç University Microphotonics Research Laboratory, for his guidance, kindness and generous help throughout my Master of Science Thesis research.

Then I would like to thank Prof. Alper Kiraz, and Asst. Prof. Onur Ferhanoğlu for participating as committee members in my thesis, and for their valuable feedback.

I would also like to thank Koç University Microphotonics Research Laboratory members; Ulaş Sabahattin Gökay, Hüseyin Ozan Çirkinoğlu, Nurperi Yavuz, Syed Sultan Shah Bukhari, Suat Kurt, and Muhammad Zakwan for their help in the laboratory and contribution to this thesis.

In addition, for their endless love and support, I would like to thank my mother, my father, my brother, Murat and my sister, Merve.

Outside of my group, I would like to thank my dearest friends, for their support and friendship. I wish to express my sincere gratitude to Zeynep Sümer for her heartfelt support and company, which composed unforgettable memories over the past years in the graduate school. I am also fortunate to have spent two delightful years with my apartment mate Onur Dereli.

Finally, I would like to acknowledge the partial support of this thesis by the Scientific and Technological Research Council of Turkey (TUBITAK) Project Grant No: 114F312.

This thesis is dedicated to my family.

TABLE OF CONTENTS

List of Tables

List of Figures

NOMENCLATURE

a	radius of sphere
a_n	transverse magnetic mode elastic scattering coefficient
α	attenuation coefficient
b	impact parameter
b_n	transverse electric mode elastic scattering coefficient
B	rms length of surface inhomogeneities on the microsphere
β_T	isothermal compressibility
c	speed of light in vacuum
D	diameter of sphere
E	electric field amplitude
ε_1	dielectric constant of material
f	focal length of lens
F	finesse of cavity
Γ	mode matching coefficient related to K
h	Planck's constant
$h_n^1(x)$	first order spherical Henkel function
I	light intensity
$j_n(r)$	spherical Bessel function of the first kind
K	arbitrary coupling parameter related to Γ
k_B	Boltzmann constant
$\boldsymbol{l}$	radial mode order
L	Fabry-Pérot cavity length
λ	incident wavelength in vacuum
λ_n	resonant wavelength in vacuum

λ_{FWHM}	full width at half maxima (FWHM) in wavelength
$\Delta\lambda_{FSR}$	free spectral range (FSR) in wavelength
$\Delta\lambda_n$	mode spacing in wavelength
$\Delta\lambda_{n,l}^{TE,TM}$	spectral shift between TE and TM polarizations of scattered light in wavelength
m	relative refractive index
$\boldsymbol{m}$	azimuthal mode number
$\boldsymbol{n}$	mode number
n_g	group refractive index
N	refractive index of the resonator
$N_{outside}$	outside refractive index
NA	numerical aperture of lens
ν_0	frequency of incident photon
ν_{vib}	vibrational frequency
$\Delta\nu_{FSR}$	free spectral range (FSR) in frequency
$\Delta\nu_n$	mode spacing in frequency
$\Delta\nu_{n,l}^{TE,TM}$	spectral shift between TE and TM polarizations of scattered light in frequency
$P_n^m(\cos\theta)$	Legendre polynomial
$\psi_{n,l,m}$	wave equation
ω_0	resonant angular frequency
$\omega_{n,l,m}$	angular frequency
Q	quality factor of a resonance
Q_{int}	quality factor associated with the internal losses
Q_{rad}	quality factor associated with the radiative losses
Q_{cont}	quality factor associated with the surface contaminant losses
Q_{mat}	quality factor associated with the bulk material losses

Q_{ext}	quality factor associated with the external losses
Q_{tot}	total quality factor
R	reflectance
ρ	photoelastic coefficient
σ	rms size of surface inhomogeneities
t	time
$\left\|t^2\right\|$	incident mode intensity coupling coefficient
T	absolute temperature
T'	transmittance
τ	lifetime of photon inside cavity
θ_i	incidence angle
θ_t	transmittance angle
θ_c	critical angle
W	stored energy
WD	working distance of lens
x	size parameter of microcavity
$z_n(kr)$	spherical Bessel function of any kind
$\varnothing$	spot size of beam

Chapter 1

INTRODUCTION

Over the past three decades, morphology dependent resonances (MDRs), the optical resonances occurring by the interaction of light with spherical microcavities of various materials such as fluidic droplets, and solid state spheres [1], were vastly investigated [2]. Spherical microcavities have diverse applications in sensing [3], filtering [4], and lasing [5] due to their high Q-factor resonances, and high concentration of modes in small cavity volumes at optical frequencies [6].

Natural modes of oscillations at specific frequencies, corresponding to precise size to wavelength ratios (size parameter) occur in dielectric and semiconductor spheres [2]. The localization of electromagnetic waves inside the microsphere is realized by total internal reflection (TIR) [7]. Microspheres provide the concave surface for light, to circumnavigate around the great circles, giving rise to whispering gallery modes (WGMs) [8]. Similarly, the quality of surface finish is essential to achieve high Q-factors up to an order of magnitude to 10^{10} [9], while confining WGMs in circular microcavities [10].

Because of its unique lattice structure, robust physical properties such as high thermal conductivity, high ignition point, and high density [11], as well as distinctive optical properties, i.e., broad transmission range from ultraviolet to far infrared (far-IR) [12], wide electronic bandgap (5.5 eV), and large Raman gain [13]; different forms of diamond were investigated for applications such as microwave antennas [14], quantum information processing [15], sensors [16], and electronics [17]. As is well known, nitrogen vacancy (NV) centers inside the diamond lattice give rise to such applications by replacing two carbon atoms by one nitrogen atom and a vacancy [18]. Two forms of NV centers can form out of the vacancy, depending on the floating electrical charge at the color center, namely NV^0 and NV^-. It is possible to control properties of this electrical charge by interactions with light, which can further be exploited around a microsphere resonator [19].

Previously, solid microcavities manufactured of materials such as glass [20], silicon [21], and germanium [22] were well studied as high Q-factor optical resonators. Diamond microcavities are now attractive, because of the recent developments in high purity diamond crystal manufacturing techniques in various geometries [23], and the possibly to alter the quantum spin state of the stable NV^- centers. Formerly, resonators manufactured of diamond with morphologies of race-track on silica [24], ring on silica [25,26], and nearly spherical with 2 mm diameter coupled to a silicon prism [27] were investigated, and their corresponding Q-factors were measured to be in the order of 10^5, 10^6 and 10^7, respectively.

In this thesis work, we report our observations of Raman scattering and photoluminescence (PL) of a 1mm synthetic diamond in spherical morphology, as well as the elastic light scattering from the WGM resonances in the same synthetic diamond microsphere by using a near-IR tunable diode laser coupled to an optical fiber half-coupler (OFHC). Our results indicate that, a 1 mm diamond microsphere has a mode spacing of 0.332 nm and the Q-factor of the resonances is measured to be on the order of 10^4 at a central wavelength of 1426.29 nm.

Chapter 2 is a brief introduction to resonators by inspecting properties of a Fabry-Pérot resonator. It also summarizes the subject of optical microsphere resonators. A description of an optical microsphere is presented, as well as the Lorenz-Mie Theory that explains the elastic scattering from a microsphere in 90^o scattering and 0^o transmission directions. This chapter also includes the portrayal of WGMs in terms of mode spacing, Q-factor, and coupling analysis together with the definitions of the size and impact parameters.

Chapter 3 presents information about diamonds in terms of physical and optical properties. Physical properties of diamonds are analyzed in terms of material properties and classification of diamond types in terms of impurities. Optical properties, such as refractive index and absorption coefficient, are discussed. Photoluminescence caused by NV centers and Raman scattering under 532 nm visible laser excitation are explained with respect to the corresponding electronic energy level transitions.

Chapter 4 includes the results of the diamond spectroscopy. The investigated diamond samples are presented along with the experimental setup, which is used to measure the PL spectra and Raman scattering. PL results of the diamond samples and manufacturing details of diamond microsphere are

included, as well as the microRaman spectra acquired by Raman microscopy. Finally, images of various diamond samples, including the diamond sphere during 532 nm laser excitation, taken by a microscope camera with a high pass color filter, are also displayed in this chapter.

Chapter 5 is about the elastic scattering of light by the diamond microsphere. The measurement setup to detect elastic scattering and transmission is shown along with the transverse electric (TE) and transverse magnetic (TM) spectra for both 90^{o} elastic scattering and 0^{o} transmission. Parameters such as Q-factor and mode spacing are analyzed, and compared with the previous reported values on diamond resonators.

Finally, chapter 6 summarizes the work done, and gives brief information about the future work, that can be conducted in this topic using diamond microcavities.

Chapter 2

OPTICAL RESONATORS

2.1 Fabry-Pérot Resonator

An optical resonator can be achieved by aligning two parallel mirrors in a manner that a light beam would successfully complete one full round-trip that satisfies a phase matching condition. The most typical form is a Fabry-Pérot resonator with a fixed linear distance, *L*, between the two mirrors, which yields a round-trip path of 2*LN*, where *N* is the refractive index of the media between the two mirrors [10]. The Fabry-Pérot resonators selectively reflect or transmit light depending on the particular wavelength. A schematic of a Fabry-Pérot resonator, which consists of a medium with refractive index N confined with two mirrors is presented in Fig. 2.1. The light propagates in different mode numbers (***n)*** during its round-trip. For a Fabry-Pérot resonator, the relation between the mode number, wavelength (λ) and round-trip is formalized by [28]:

$$n\lambda = 2LN \tag{2.1}$$

The resonance exhibits itself when, there is an integer mode number for a round-trip. Eq. (2.1) is satisfied when, the light waves interfere constructively by forming a standing electromagnetic wave between the spacing of two mirrors. Resonant peaks arise in the corresponding resonance spectra at the particular λ due to the constructive interferences for their respective ***n****'s*.

The dependence of the round-trip length to the wavelength is characterized by a dimensionless size parameter (*x)*, which relates the round- path length to the wavelength of the incident light by [28]:

$$x = \frac{2L}{\lambda / N_{outside}} \tag{2.2}$$

that can be further converted into a relation between mode number *n* and reflective index *N* by

$$n = \frac{N}{N_{outside}} x = mx \quad (2.3),$$

where m is the relative refractive index of the inside medium.

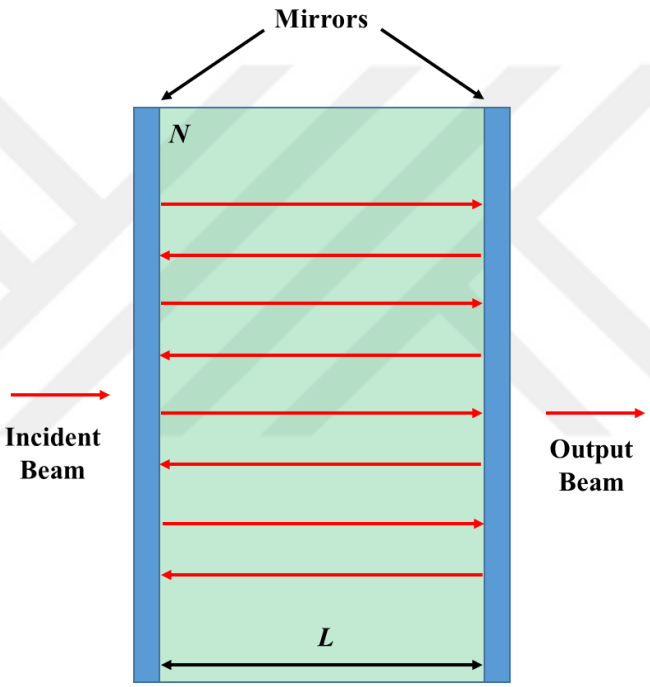

Fig. 2.1 Schematic of a Fabry-Pérot Resonator with a spacing of *L* and refractive index of *N*.

By changing in the spacing or the refractive index between the mirrors, it is possible to alter the resonant wavelengths, which indicates Fabry-Pérot resonators as sensitive wavelength selective devices, that give rise to various applications such as sensors and laser cavities [29].

2.1.1 Free Spectral Range

The resonance condition is satisfied by infinite number of modes inside the cavity, that are separated by a fixed spacing due to the quantized state of the modes. The distance between two resonant peaks are identified as free spectral range (FSR) and can be defined in terms of frequency as:

$$\Delta\nu_{FSR} = \Delta\nu_{n+1} - \Delta\nu_n = \frac{c}{2LN} \quad (2.4),$$

where c is the speed of light in vacuum. In terms of wavelength for two consecutive modes ***n*** and ***n***+1, that satisfy the resonance condition defined in Eq. (2.1). The assumption of $\boldsymbol{n} \approx \boldsymbol{n}+1$ can be made for high mode numbers of ***n***, which can modify the term as:

$$\Delta\lambda_{FSR} = \frac{\lambda}{\nu}\Delta\nu_{FSR} = \frac{\lambda^2}{2LN} \quad (2.5),$$

at the central resonant wavelength λ. As is clear from the Eqs. (2.4) and (2.5), FSR decreases as the spacing between the mirrors increases, as well as the refractive index of the media in between the mirrors of a Fabry-Pérot resonator.

2.1.2 Q-Factor

Quality factor (Q-factor) is another significant parameter that defines a resonator. At the resonant wavelengths the Fabry-Pérot resonator, or any other resonator, transmits 100% of the incident beam by neglecting the reflectance (*R)* of the mirrors. Theoretically, Q-factor can be defined as:

$$Q = 2\pi \frac{stored\ energy}{energy\ loss\ per\ cycle} \quad (2.6),$$

which is also the ratio of the resonant wavelength to the full-width-at-half-maxima (FWHM) of the resonance peak and shown as:

$$Q = \frac{\lambda}{\lambda_{FWHM}} \quad (2.7),$$

where λ_{FWHM} represents the FWHM of the peak. Q-factor defines the sharpness of the resonant peak and is in a correlation with *R* of the Fabry-Pérot resonator's mirrors. Reduction in the Q-factor occurs, when an energy loss at the cavity is realized. This is dependent on various factors such as reflectance, mirror

surface absorption. Q-factor is also known as the resolving power of the resonator, and high Q-factor values are essential for different applications, i.e., laser cavities, monochromatic separations of wavelengths, or frequency comb generations [30].

2.1.3 Finesse

The ratio of FSR to FWHM of a resonant peak defines the finesse (*F)* of the resonator and is shown as:

$$F = \frac{\Delta\lambda_{FSR}}{\lambda_{FWHM}} \tag{2.8}.$$

Finesse of an ideal Fabry-Pérot resonator can also be defined by:

$$F = \frac{\pi\sqrt{R}}{1-R} \tag{2.9}.$$

Finesse is entirely defined by the cavity losses, and has no relation with the resonator length. High finesse can be achieved by increasing *R* of the mirrors. The relation between Q-factor, finesse, and reflectance are realized by

$$Q = \frac{\lambda}{\Delta\lambda_{FSR}} F = nF = \frac{2Lm\pi\sqrt{R}}{\lambda(1-R)} = \frac{mx\pi\sqrt{R}}{1-R} \tag{2.10}.$$

Eq. (2.10) yields an understanding of the dependency of the Q-factor to reflectance of the Fabry-Pérot mirrors, size parameter, and the relative reflective index of the media. As can be realized from Eq. (2.10) higher mode numbers will yield high Q-factors, hence incident waves with wavelengths, which corresponds to higher mode numbers can exhibit higher Q-factors.

Fig. 2.2 illustrates a transmission spectrum of a Fabry-Pérot Resonator. λ_{FSR} and λ_{FWHM} are shown on the figure along with the resonance wavelengths λ_{n-1}, λ_n, and $\lambda_{n+1.}$ Intensity has arbitrary units and

normalized with I/I_{max}. FSR is defined as the free spectral range between two resonant modes, that satisfy Eq. (2.4) and (2.5), as shown on the spectrum.

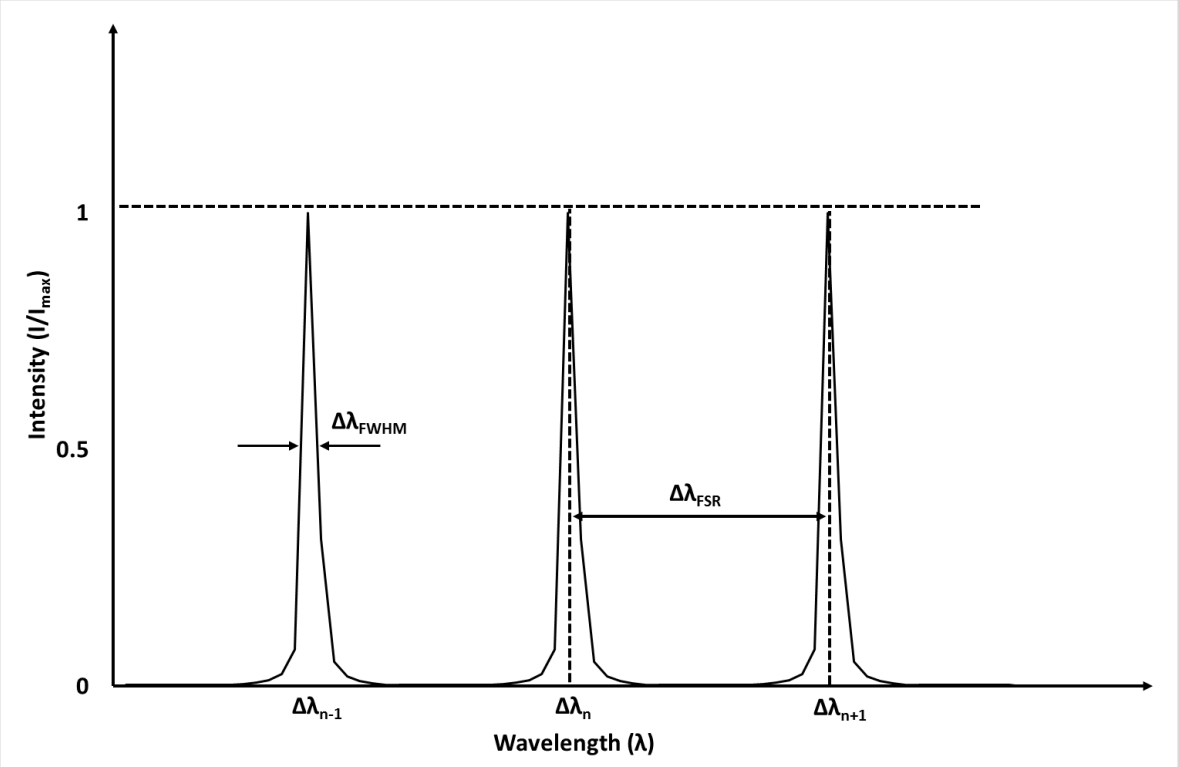

Fig. 2.2 Transmitted light intensity of the Fabry-Pérot resonator modes.

2.2 Spherical Microcavity Resonator

Similar to Fabry-Pérot resonators, incident light beam should complete a full round trip to exhibit morphology dependent resonances (MDR) inside the spherical microcavity. The circumnavigating light is confined inside the sphere by exploiting the total internal reflection (TIR). TIR is defined by the boundaries obtained from the Snell's Law as

$$N_{outside} \sin\theta_i = N \sin\theta_t \quad (2.11),$$

where $N_{outside}$ and θ_i are the refractive index and angle of incidence in the incident media, and N and θ_t are the refractive index and the transmittance angle after the plane of incidence. TIR is realized if the incident angle is greater than the critical angle θ_c ($\theta_i > \theta_c$) that is defined by

$$\theta_c = \sin^{-1} \frac{N}{N_{outside}} \quad (2.12).$$

The localization of propagating electromagnetic waves inside the microsphere is realized by total internal reflection (TIR). Microspheres provide the concave surface for light to circumnavigate around the microcavity, giving rise to whispering gallery modes (WGMs) [31]. Localization of WGMs due to TIR are presented in Fig. 2.3.

Coupling of light to the microcavity can be achieved by a waveguide or a prism that carries propagating light in the vicinity of the microsphere. A standing wave occurs in the cavity, whenever the incident beam with wavelength λ in $N_{outside}$ is in phase with the reflected light. This resonance condition can be formalized as defining the round trip around the sphere by

$$n\lambda = 2\pi aN \quad (2.13),$$

where $\boldsymbol{n}$ is the mode number, λ is the wavelength of the incoming light, a is the radius of the microsphere and N is the refractive index of the microcavity. Similar to Fabry-Pérot resonator, $\boldsymbol{n}$ is an integer that defines the polar angular quantum mode number, and λ/N defines the wavelength of the resonating light inside the cavity.

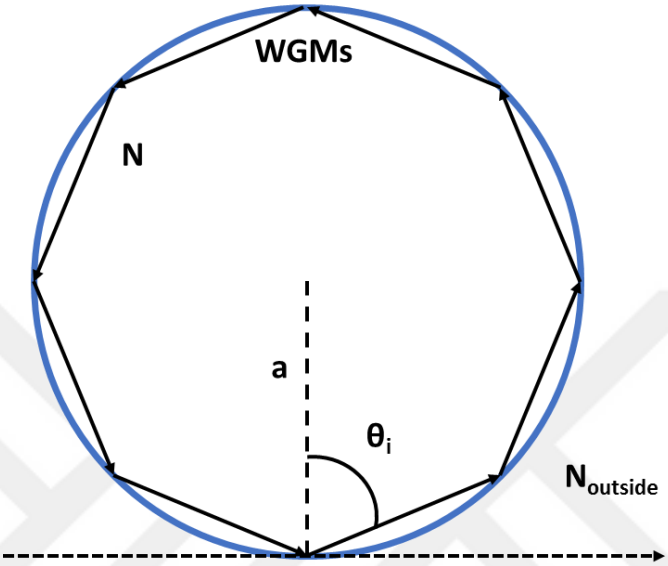

Fig. 2.3 Propagation of light around a microsphere exhibiting WGMs with TIR.

A dimensionless size parameter that compares the wavelength and circumference of the sphere can be formalized by [32]:

$$x = ka = \frac{2\pi a}{\lambda / N_{outside}} \tag{2.14},$$

where x is the size parameter, and k is the propagating wave vector in the surrounding medium $N_{outside}$. A relative refractive index m, should be defined to express the resonance condition

in terms of size parameter.

$$m = \frac{N}{N_{outside}} \tag{2.15},$$

is the relative refractive index. By joining Eq. (2.14) and (2.15), x can be expressed by

$$n \geq x \geq \frac{nN_{outside}}{N} = \frac{n}{m} \qquad (2.16),$$

in terms of mode number and relative refractive index. The right side of the Eq.(2.16) is similar to the case of the one-dimensional Fabry-Pérot solution, shown in Eq. (2.3), for minimum mode order $l = 1$. The left side of the Eq. (2.16) is for maximum mode order $l = l_{max}$.

2.2.1 Lorenz-Mie Theory for Elastic Scattering from Microspheres

Different forms of modes exhibit themselves during the propagation of light inside around a microsphere. These modes are geometry dependent and defines the wave nature of the light during its one round trip in its three dimensional freedom.

The notational difference between electromagnetic (EM) wave theory and quantum mechanics (QM) theory is presented in Table 2.1 for azimuthal mode number ***m***, polar mode number ***n***, and radial mode order ***l***. The azimuthal mode number ***m*** shows the number of azimuthal maxima of the intensity distribution inside the sphere in the range between 0^o and 180^o, where ***l*** represents the number of intensity maxima in the radial direction [33]. For each polar mode, the allowed azimuthal mode numbers are in between $-\boldsymbol{n} < \boldsymbol{m} < \boldsymbol{n}$, that gives rise to $2\boldsymbol{n}+1$ degeneracy of the azimuthal modes [8,34].

Table 2.1. Mode Notations in Electromagnetics (EM) & Quantum Mechanics (QM)

Parameter	EM Notation	QM Notation
Azimuthal mode number	***m***	***m***
Polar mode number	***n***	***l***
Radial mode order	***l***	***n***

Considering a perfect sphere, with minimal elipticity, all of the ***m*** modes are 2***n***+1 degenerate, however the degeneracy is dependent on the symmetry at the z-axis, and can be lifted based on the deformations of the geometry of the sphere. On the other hand, MDRs are independent of the direction of the light circumnavigating the sphere. In the case of high resolution measurements, it is possible to observe a mode splitting due to internal backscattering caused by ***m*** modes, which couples two counter propagating modes to the spherical microcavity.

Light interaction with a microcavity to exhibit MDRs can be fully described by electromagnetic theory. Helmholtz equation for electromagnetic spherical boundary conditions were first solved by Mie [35]. Mie scattering is a description for light scattering from spheres, that has a size parameter between ~ $0.1 < x < 100$. Solution of such an electromagnetic problem requires detailed derivations, however only the crucial equations are mentioned in this thesis. Helmholtz eigenvalue equation is given by

$$\nabla^2 \psi_{n,l,m} + \left(\frac{\omega^2_{n,l,m}}{c^2(\vec{r})} \right) \psi_{n,l,m} = 0 \qquad (2.17),$$

where $\psi_{n,l,m}$ is the eigenfunction, $\omega^2_{n,l,m}$ is the eigenvalue for the $-c^2(\vec{r})\nabla^2$ operator.

Assuming an incident plane wave approaching a microsphere to excite the MDRs, it is possible to define the eigenmodes of the characteristic equations satisfying the wave equation in spherical polar coordinates as

$$\psi_{emn} = \cos(m\phi) P_n^m(\cos\theta) z_n(kr) \qquad (2.18),$$

and

$$\psi_{omn} = \sin(m\phi) P_n^m(\cos\theta) z_n(kr) \qquad (2.19),$$

where $P_n^m(\cos\theta)$ is the Legendre polynomials with degree *n* and order *m*, and $z_n(kr)$ demonstrates any of the spherical Bessel functions, thus the vector spherical harmonics of the propagating plane waves is expressed by

$$\overrightarrow{E_i} = E_o \sum_{n=1}^{\infty} i^n \frac{2n+1}{n(n+1)} (\overrightarrow{M}_{o|n}^{(1)} - \overrightarrow{N}_{e|n}^{(1)}) \quad (2.20),$$

where $\overrightarrow{M}_{o|n}^{(1)} = \vec{\nabla} \times (\vec{r}\psi_{o|n})$ and $\overrightarrow{N}_{e|n}^{(1)} = \frac{\vec{\nabla} \times \overrightarrow{M}_{e|n}^{(1)}}{k}$ [34, 36]. Considering an isotropic and homogenous microsphere with radius (a), elastically scattered field is expressed by

$$\overrightarrow{E} = \sum_{n=1}^{\infty} E_n (a_n i \overrightarrow{N}_{e|n}^{(3)} - b_n \overrightarrow{M}_{o|n}^{(3)}) \quad (2.21),$$

where a_n and b_n are the elastic scattering coefficients, which can be further simplified by the Riccati-Bessel functions

$$\psi_n(r) = r j_n(r) \text{ and } \xi(r) = r h_n^{(1)}(r) \quad (2.22)$$

where $j_n(r)$ and $h_n^{(1)}(r)$ are the Bessel and spherical Henkel functions of the first kind, respectively. As a result the elastic scattering coefficients for TM and TE polarizations are formalized as [8,34]

$$a_n = \frac{\psi_n^{'}(Mx)\psi_n(x) - M\psi_n^{'}(x)\psi_n(Mx)}{\psi_n^{'}(Mx)\xi_n(x) - M\psi_n(Mx)\xi_n^{'}(x)} \quad (2.23),$$

and

$$b_n = \frac{M\psi_n^{'}(Mx)\psi_n(x) - \psi_n^{'}(x)\psi_n(Mx)}{M\psi_n^{'}(Mx)\xi_n(x) - \psi_n(Mx)\xi_n^{'}(x)} \quad (2.24),$$

respectively.

Eqs. (2.23) and (2.24) are applicable for planar waves, however we are using an optical fiber half coupler (OFHC) carrying a light beam with a Gaussian distribution. Nominators of these equations should be altered to satisfy the condition for a guided wave [37]. The denominators of the elastic

scattering equations will not change, since the resonances exhibit themselves at the poles of the transfer function of elastic scattering from a microsphere.

There are two elastic scattering coefficients, that corresponds to the solutions for the modes of light with transverse electric (TE) and transverse magnetically (TM) polarized lights, respectively.

The two schools of solutions of the EM Helmholtz equation for TE and TM polarizations are analogous to the energy levels of a QM problem similar to the notations shown in Table 2.1. Therefore MDRs are defined with quantized polar, radial, and azimuthal numbers, ***n***, ***l,*** and ***m***, respectively.

2.2.2 Mode Spacing

Similar to the Fabry-Pérot resonator a constant range between two resonant peaks is present for WGMs confined in a spherical microcavity. Previously, this gap was called as free spectral range (FSR) for a Fabry-Pérot resonator as shown in Fig. 2.2, since there are no extra signal in between λ_n and λ_{n+1} due to an additional modes, unless transverse modes are apparent. The range is not as free as a Fabry-Pérot for a microsphere resonator, thus it would be more accurate to name this gap as Mode Spacing in terms of terminology.

As formalized for Fabry-Pérot, mode spacing can be expressed as the difference between two consecutive polar modes ***n*** for the identical radial mode order ***l***, first for size parameter as:

$$\Delta x_n = x_{n+1} - x_n \tag{2.25},$$

where Δx_n is the distance between two consecutive modes ***n***+1 and ***n***, by assuming the size parameter as $x+\Delta x$ and x for terms the ***n***+1 term for ***n***, respectively. Δx mode spacing is then given as:

$$\Delta x = \frac{x \tan^{-1} \sqrt{\left(\frac{mx}{n}\right)^2 - 1}}{n \sqrt{\left(\frac{mx}{n}\right)^2 - 1}} \tag{2.26},$$

where m is the relative refractive index and x the size parameter. By assuming $x >> 1$, $x \sim \boldsymbol{n}$, $mx \sim \boldsymbol{n}$ and $mx > \boldsymbol{n}$, it is possible to simplify Eq. (2.26) as [38]:

$$\Delta x = \frac{\tan^{-1}\sqrt{m^2-1}}{\sqrt{m^2-1}} \tag{2.27}.$$

This term is almost independent of the size parameter x, if $\boldsymbol{n}$ and x are sufficiently large, and only a function of the relative refractive index m. Recall Eq. (2.14), that defines the size parameter, $x = 2\pi a N_{outside}/\lambda$, and replace x and λ with the corresponding consecutive mode orders as $\Delta x_{n+1} = 2\pi a/\lambda_{n+1}$ and $\Delta x_n = 2\pi a/\lambda_n$. Then the size parameter mode spacing at Eq. (2.25) can be defined in terms of wavelength by:

$$\Delta x = \frac{2\pi a N_{outside}\left(\Delta\lambda_n\right)}{\lambda_n^2} \tag{2.28},$$

where $\Delta\lambda_n = \lambda_{n+1} - \lambda_n$ is the mode spacing in terms of wavelength, and $\lambda_n^2 = \left(\lambda_{n+1}\right)\left(\lambda_n\right)$ by assuming $\boldsymbol{n}+1 \approx \boldsymbol{n}$ for the high mode numbers, $1 \ll \boldsymbol{n}$. Finally, to define the wavelength mode spacing Eq. (2.27) and (2.28) are collated as [39]:

$$\Delta\lambda_n = \frac{{\lambda_n}^2 \tan^{-1}\sqrt{m^2-1}}{2\pi a\, \mathrm{N}_{\mathrm{outside}}\sqrt{m^2-1}} \tag{2.29},$$

where λ_n is the resonant wavelength, m the relative refractive index and a the radius of the microsphere.

Another approach is to define the mode spacing in frequency domain. Similar to Eq. (2.4) for Fabry-Pérot $\Delta\nu$ for the spherical resonator is given as:

$$\Delta\nu = \Delta\nu_{n+1} - \Delta\nu_n \tag{2.30}.$$

The frequency at the corresponding mode can be calculated via the roundtrip as presented in Eq. (2.14), thus the ν for $\boldsymbol{n}$ and $\boldsymbol{n}+1$ modes are shown by:

$$\nu_n = \frac{nc}{m2\pi a} \tag{2.31},$$

where c is the speed of light in the vacuum. By subtracting the term given in Eq. (2.31) according to Eq. (2.30) and Eq. (2.27), mode spacing in terms of frequency can be expressed as:

$$\Delta\nu_n = \frac{c}{2\pi a}\frac{\tan^{-1}\sqrt{\left(m^2-1\right)}}{\sqrt{\left(m^2-1\right)}} \tag{2.32},$$

for the same polarization.

It is more accurate to select Eq. (2.26) or (2.32) to calculate the mode spacing, if the assumptions of $x >> 1$, $x \sim \boldsymbol{n}$, and $mx \sim \boldsymbol{n}$ are not satisfied. To be more precise, $|x-n| \gg \frac{1}{2}$ and $|x-n| \geq 4$ defines the conditions to use Eq. (2.26) to calculate the mode spacing with %1 accuracy, and if $|x-n| < 4$ then Eq. (2.29) can predict the mode spacing with the same accuracy [40].

2.2.3 Q-Factor

Q-factor is a dimensionless parameter, which is used to define how long a photon can be confined inside an optical microcavity. Q-factor can be expressed by the average lifetime of photon in the resonant light mode as $\tau = Q/\omega_o$, where τ is the average photon lifetime, and ω_o the resonant angular frequency.

On the other hand, Q-factor of a WGM resonance is the ratio of the stored energy to the energy lost during one period as shown in Eq. (2.6) similar to a Fabry-Pérot resonator, which can be also given as [41]:

$$Q = \frac{2\pi W}{\left(-\frac{dW}{dt}\right)\left(\frac{2\pi}{\omega_0}\right)} = -\frac{\omega_o W}{dW/dt} \tag{2.33},$$

where W is the stored energy, $-dW/dt$ the power dissipation, ω_o the resonant angular frequency, and $2\pi/\omega_o$ the period of the resonance. It is possible to formalize the stored energy W, as a function of Q-factor by:

$$W(t) = W_o \exp\left(\frac{-\omega_o t}{Q}\right) \tag{2.34}.$$

Electric field inside a microcavity can be expressed in terms of Q-factor by:

$$E(t) = E_o \exp\left(i\omega_o t\right)\exp\left(\frac{-\omega_o t}{Q}\right) \tag{2.35},$$

which yields the energy in the cavity near a resonant frequency using the EM theory by:

$$\left|E(\omega)\right|^2 \propto \frac{1}{\left(\omega-\omega_o\right)+\left(\frac{\omega_o}{2Q}\right)^2} \tag{2.36}.$$

Resonances exhibit themselves in Lorentzian lineshapes as sharp peaks at the resonant wavelengths. At the full-width-half-maximum (FWHM) energy of the resonant field in Eq. (2.36), a condition of $\left|\omega-\omega_o\right| = \omega_o / 2Q$ occurs, thus it is possible to measure the Q-factor from the lineshape with Eq. (2.7).

Optical microsphere resonators are dissipative cavities due to various loss mechanisms. Dependence of the Q-factor to such intrinsic dissipations are formalized as [42]:

$$Q_{\text{int}}^{-1} = Q_{rad}^{-1} + Q_{ss}^{-1} + Q_{mat}^{-1} + Q_{cont}^{-1} \tag{2.37},$$

where Q_{rad} is due to intrinsic radiative losses, Q_{cont} caused by surface contaminants, Q_{ss} scattering losses due to residual surface inhomogeneities, and Q_{mat} due to material loss.

The main source of radiative losses is the imperfect nature of TIR from a spherical (curved) surface. The concave surface of a microsphere causes the evanescent field of the light to propagate, thus the

photons tunnel out of their bound state. A portion of the energy escapes the potential barrier and Q_{rad} can be expressed by a semiclassical approximation to the Riccati-Bessel functions as [43]:

$$Q_{rad} = x\exp\left(2\left(l+\frac{1}{2}\right)g\left(\frac{x}{l+\frac{1}{2}}\right)\right) \tag{2.38}$$

where $g(y) = -\sqrt{1-y^2} + \arg\cosh\left(1/y\right)$, x the size parameter and $\boldsymbol{l}$ the radial mode order. Q_{rad} diminishes as a high number of propagating modes are confined with TIR inside the microsphere. Numerically, this boundary can be defined by D/λ, where D is the diameter of the spherical microcavity, and λ the incident wavelength. If $D/\lambda \geq 15$, a Q_{rad} greater than 10^{11} can be achieved, therefore Q_{rad}^{-1} will diminish and another intrinsic energy dissipation will limit the Q-factor.

Loss due to surface inhomogeneities are estimated based on the model of Rayleigh scattering by molecular-sized surface clusters under laser excitation on the edge confined with TIR by [42,44]:

$$Q_{ss} = \frac{\lambda^2 a}{\pi^2\sigma^2 B} \tag{2.39}$$

where σ is the rms size, B the correlation length of the surface inhomogeneities, and a the radius of the microsphere. Q_{ss} is dependent to the radius of the sphere, thus high Q-factors can be only achieved by large enough microspheres, i.e., larger than 100 μm [42]. σ and B are generally on nm scale depending on the purity of the microsphere surface.

The other loss is caused by the material absorption and bulk elastic (Rayleigh) scattering losses. Q_{mat} is expressed as [42]:

$$Q_{mat} \approx \frac{2\pi m}{\alpha\lambda} \tag{2.40}$$

here m is the relative refractive index, λ the incident wavelength and α the attenuation coefficient, that is dependent on the absorption coefficient of the material at the corresponding wavelength [45]. Scattering

loss coefficient in glasses is due to the microscopic variations in the local dielectric constants associated with the random molecular structure of the material, thus can be formalized by [46]:

$$\alpha_{scat} = \frac{8}{3}\frac{\pi^3}{\lambda^4}\left(m^8\rho^2\right)\left(k_B T\right)\beta_{\mathrm{T}} \tag{2.41},$$

where ρ is the photoelastic coefficient, k_B the Boltzmann constant, T absolute temperature, and β_T the isothermal compressibility of the material. α_{scat} will then yield the bulk Rayleigh scattering loss to calculate Q_{mat}.

Q_{cont} represents the losses due to surface contaminants occurring during the manufacturing process of the microsphere. The influence of the water contaminants introduced to the silica (SiO_2) microspheres during their fabrication process, and their limitation to the Q-factor were previously observed [42].

2.2.4 Coupling Analysis

Previously, the intrinsic contributions to the Q-factor were discussed, but the total Q-factor is also dependent on the external loses as well, thus is given as:

$$Q_{tot}^{-1} = Q_{\mathrm{int}}^{-1} + Q_{ext}^{-1} \tag{2.42}.$$

Q_{ext} is induced by the coupling of light from a waveguide or a silicon prism. Compared to the other intrinsic contributions to the Q-factor, Q_{ext} is due to a external loading, and can be expressed by [47]:

$$Q_{ext} = \frac{2\pi x}{\left|t^2\right|} = \frac{\left(2\pi\right)^2 ma}{\lambda\left|t^2\right|} \tag{2.43},$$

where x is the size parameter as defined in Eq. (2.14), and t is the incident light mode field coupling coefficient from the fiber to the diamond microsphere. t is a purely imaginary value, and is generally estimated to be $\left|t^2\right| << 1$ for optical half couplers and tapered fibers by considering the coupling of a single mode propagating in the fiber to one of the resonant modes in the diamond microsphere [47].

A Q-factor, that has an order of magnitude greater than 10^8 can be achieved, depending on the value of *t*, thus the term Q_{ext}^{-1} in Eq. (2.42) can diminish, relative to Q_{int}.

Fig. 2.4 illustrates the coupling of an incident beam propagating in a waveguide to a microsphere. *a* and *b* are the radius and the impact parameter, respectively. The transmittance can be expressed by [48]:

$$T' = \left(\frac{1-K}{1+K} \right)^2 \tag{2.44},$$

where *K* is an arbitrary coupling parameter.

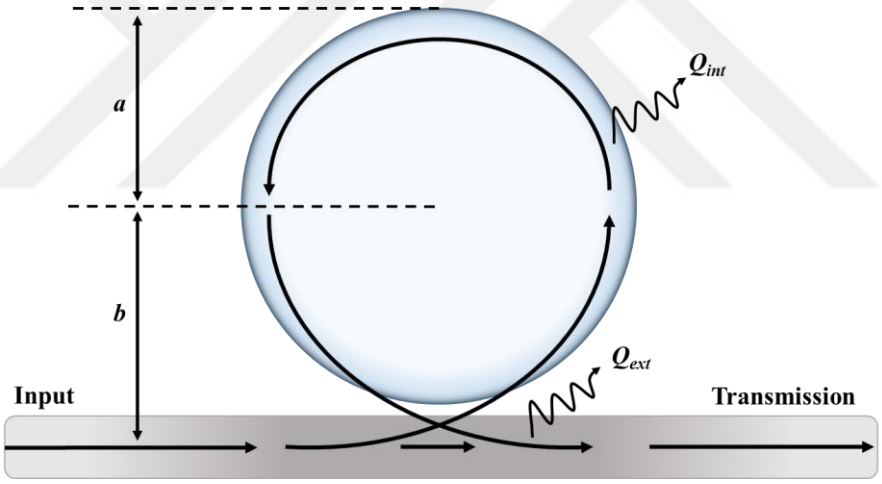

Fig. 2.4 Coupling scheme of the propagating light inside a waveguide to a microsphere.

The coupling parameter is depending on the intrinsic and extrinsic Q-factors as [49]:

$$K = \frac{4Q_{\text{int}}Q_{ext}\Gamma^2}{\left(Q_{\text{int}} + Q_{ext}\right)^2} \tag{2.45},$$

where Γ is defined as the mode matching coefficient as $\Gamma \leq 1$. It is advised to operate with a single mode coupler to achieve perfect mode matching, $\Gamma = 1$, at around the desired wavelengths.

If $Q_{ext} = Q_{int,}$ it is possible to observe a critical coupling from the waveguide to the microsphere to exhibit MDRs, hence the coupling coefficient will be $K = 1$. A non-ideal case of matching will occur, if Q_{int} exceeds Q_{ext}.

It is possible to control the loss exert due to coupling by controlling the impact parameter b, which is defined by:

$$b = \left(n + \frac{1}{2} \right) \frac{a}{x} \tag{2.46},$$

which can be defined by the mode number $\boldsymbol{n}$, and size parameter x. The impact parameter of the incident beam is restricted by $a \leq b \leq ma$ to satisfy the localization principle. Only the light rays possessing an impact parameter within the corresponding range are allowed to couple to a microsphere to exhibit WGMs. The impact parameter is illustrated in Fig. 2.5 for a microsphere with radius a, which is in contact with an optical fiber half coupler (OFHC).

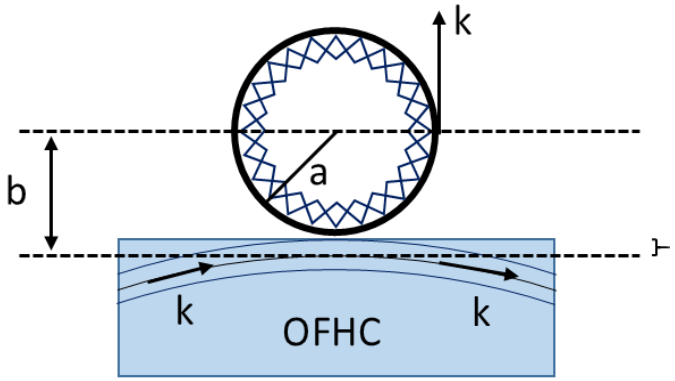

Fig. 2.5 Impact parameter illustration of a microsphere in contact with an OFHC.

Chapter 3

DIAMOND

3.1 Physical Properties of Diamond

Diamond is known as being one of the hardest materials in nature, which has important mechanical and optical properties such as hardness, large energy gap, large thermal conductivity, high carrier saturation velocity, and chemical, and radiation hardness. The robustness of this extraordinary gemstone has given rise to various products.

3.1.1 Material Properties

Previously, it was very expensive to work with, and shape diamond samples. With the development of the appropriate technology, it is now possible to grow diamond structures in laboratory environment by high pressure high temperature technique (HPHT) or chemical vapor deposition (CVD) method [23]. As is well known, a diamond lattice consists of tetrahedral carbon – carbon bonds, when compared to graphite, which is a different lattice form of carbon atoms bonded to each other by exhibiting a layered hexagonal honeycomb structure, as shown in Fig. 3.1 [50].

The closed structure of the diamond gives rise to many robust physical properties. For instance, Knoop hardness test is a microhardness test method, which indicates the hardness of small samples, and thin layers. Knoop hardness of the diamond is measured to be on the order of $10^5 \, kg \cdot mm^{-2}$ [51].

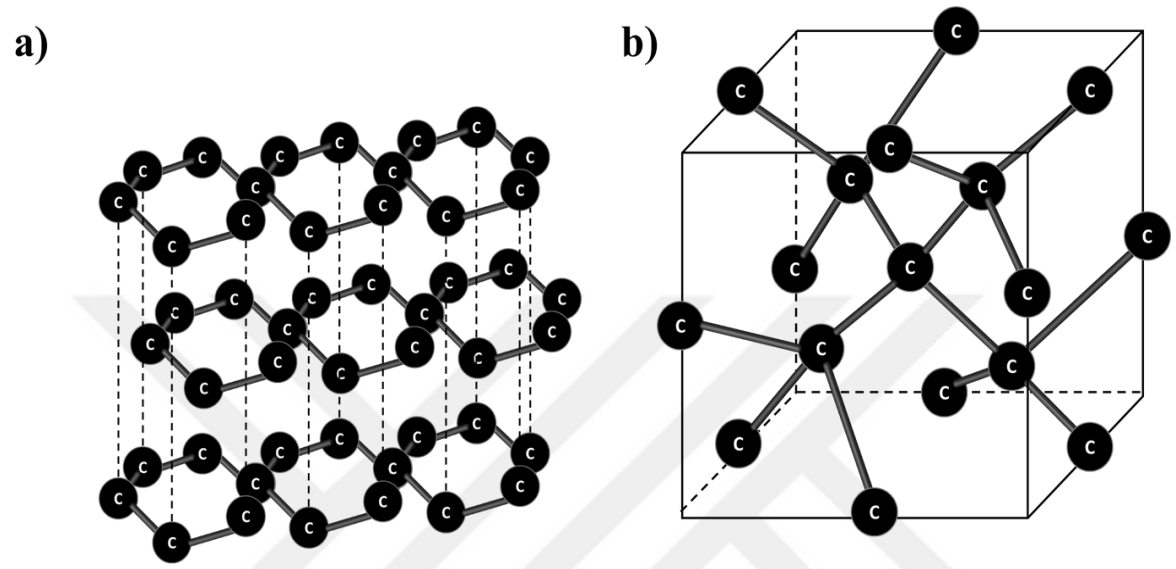

Fig. 3.1 Lattice structures formed by carbon atoms of (a) graphite and (b) diamond.

On the other hand, thermal conductivity of diamond is much higher compared to other materials. Previously, the thermal conductivity of is measured as 3320 $W \cdot m^{-1}K^{-1}$, and 1200 $W \cdot m^{-1}K^{-1}$ for carbon enriched diamond, and for CVD synthetic diamond, respectively [52]. The thermal diffusivity of diamond was also measured to be around 12.2 cm^2s^{-1} [52].

The rest of the physical parameters of a typical diamond sample are tabulated in Table 3.1 [53]. It is possible to comprehend the robustness of a diamond sample by checking the parameters in this table, such as Young's Modulus, bend strength, and fracture toughness. Also the electrical resistivity of diamond has an important role. It is possible to control the spin state of the floating electrons in the nitrogen vacancy (NV) sites (discussed in the next section) using electrical current, hence the resistivity aids the stability of such a measurement system.

All of these mechanical properties of diamonds were exploited for various physical applications in forms of thick and thin films [54].

Table 3.1. Summary of the Physical Properties of Diamond.

Physical Property	Value	Unit
Density	3.50	g/cm^3
Young's Modulus	1050	GPa
Bend Strength	850	MPa
Fracture Toughness (K_{1c})	3.50	$MPa.m^{0.5}$
Hardness	45	GPa
Thermal Expansion Coefficient	1.10	$x10^{-6}/ºC$
Coefficient of Friction	0.02	N/A
Electrical Resistivity	$> 10^{13}$	Ω.cm
Decomposition Temperature in Nitrogen	1500	ºC

3.1.2 Types of Diamonds

Nitrogen vacancy (NV) centers inside the diamond lattice give rise to many applications by replacing two carbon atoms by one nitrogen atom and a vacancy, that yields a floating electron at the NV center. There are two types of NV centers depending on the charge of the vacancy site, namely NV^0 and NV^-[55]. Not only the nitrogen (N) atoms, but also different types of atoms such as silicon (Si), boron (B), and hydrogen (H) can blend inside the diamond lattice during the formation of the sample.

Diamonds are classified into different types depending on the kind and amount of the impurities. First, diamonds are separated into two groups, Type I and Type II, based on the concentration of nitrogen impurity inside the diamond structure. A sample is classified as Type I, if the main impurity is N, and the density of N atoms are < 0.1% of all atoms inside the diamond.

Type I is divided into two groups as Type Ia and Type Ib, depending on the form of the N atoms inside the lattice. When the N atoms are present as pairs or small groups, also known as aggregates, that diamond is then classified as Type Ia. Most of the natural diamonds (more than 98% of all diamonds) are Type Ia. It is possible to imagine such aggregates inside the diamond, if one can consider a natural diamond, which confronts high amounts of pressure and temperature, along with N atoms during its formation process in the nature. A stochastic distribution of N atoms are expected in such a diamond lattice, that has a high probability of finding N atoms in small groups [12].

On the other hand, Type Ib denotes the presence of N atoms inside the diamond structure as isolated atoms. Type Ib consists 0.1% of all diamonds. N atoms are > 5 parts per million (ppm) in Type Ib diamonds, and are not structured in clusters inside the lattice. Generally, Type Ib is observed as an outcome of growing techniques of diamonds either with CVD or HPHT. Nowadays, it is possible to seed the point defects of N atoms inside the diamond both intentionally and inadvertently during its growth, thus yielding a Type Ib diamond, which depends on the concentration of N atoms [56].

Diamonds are classified as Type II, if there are no significant amounts of nitrogen present. Similarly, a nitrogen density of < 5 ppm denotes a Type II diamond. Again, Type II is divided into two subgroups as Type IIa and Type IIb. Type IIa represents the samples with no significant impurity, and is the purest among all diamonds, hence is the hardest to mine. Only 1% of all diamonds are of Type IIa, and have different colors such as brown, orange, purple, and pink caused by the small impurities induced by different atoms rather than N [57].

Finally, Type IIb represents the samples with no significant nitrogen impurity, and containing boron (B) as impurities. Only 0.1% of all the diamonds are of Type IIb, therefore they are very unique. B atoms cause the sample to have a faint blue color [12]. Diamond types and their lattice schematics are given in Table 3.2.

Table 3.2. Classification of Diamonds and Their Lattice Schematic.

Types		Definition	Lattice
Type I	Type Ia	has > 5 ppm N atoms as clusters	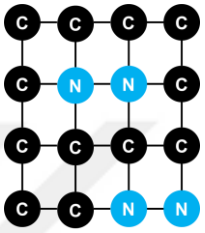
	Type Ib	has > 5 ppm N impurity as isolated atoms	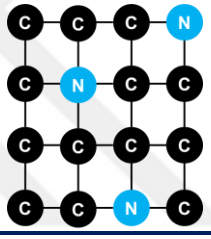
Type II	Type IIa	has < 5 ppm N atoms and no significant impurities	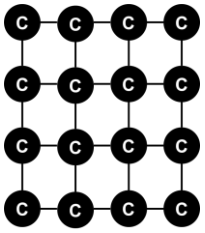
	Type IIb	has < 5 ppm N atoms and B atoms are present	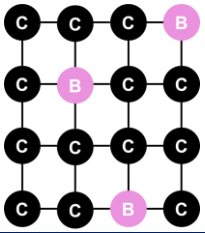

3.2 Optical Properties of Diamond

Diamond is a unique gemstone, that poses various optical properties with the aid of the impurities within the diamond lattice, i.e., its broad transmission range from ultraviolet (UV) to far-infrared (far-IR) [12], wide electronic bandgap, and large Raman gain [13]. Different forms of diamond were vastly investigated for various applications. Diamond has a large energy gap between its valance and conduction bands, which is 5.5 eV, that corresponds to 225 nm in terms of wavelength in the UV regime [58]. It is possible to observe different transitions in this bandgap via NV centers. This property of diamond will be further discussed in this chapter.

3.2.1 Refractive Index

Refractive index of a medium is wavelength dependent, so it is wiser to investigate the refractive index of Type I diamonds in the visible and the near-infrared (near-IR) region, separately. Diamond has a refractive index of 2.4250, if a 532 nm excitation source is considered to observe the index in the visible spectrum [59]. The group index n_g at the corresponding wavelength is 2.4955, while the chromatic dispersion relation is given by $\frac{dn}{d\lambda} = -0.13242\ \mu m^{-1}$ at the visible regime [60]. Around the wavelength of 150 nm, diamond has a refractive index peak value of 3.47, and an exponential decay in the index of refraction is observed starting from 150 nm to IR [61].

Furthermore, the refractive index in the near-IR region at around 1427 nm was previously found as 2.3879 [61,62]. The group index is n_g = 2.3895, and the dielectric constant is ε_1 = 5.7022 at the corresponding wavelengths. From the diamond refractive index of data from extreme UV to near-IR, the refractive index of diamond at near-IR is 2.38 around the photon energy of 1 eV [61].

3.2.2 Absorption Coefficient

Infrared absorption of diamond varies from sample to sample depending on the impurity center induced by the element, which infiltrated the diamond lattice, as well as the phonons. Absorption

coefficient spectrum of a hydrogen induced natural diamond in the mid-IR shows the effect of the lattice impurities on the absorption [63]. The extra C-H bonds exhibit IR absorption, that alters the absorption coefficient of regular C-C bonds [64].

Absorption spectrum of an H rich natural diamond sample [63] also illustrates the influence of the concentration of the impurities. The increment of additional bonds, rather than C-C, will alter the absorption coefficient. Two absorption coefficient spectra of synthetically grown Type Ib diamond samples with different amount of N concentrations at near-IR regime were studied [65-66]. The Near-IR absorption coefficient spectrum of Type Ib diamond samples at 1427 nm is measured to be < 5 cm^{-1} at room temperature with NV center concentration of 270 ppm [65]. However, for the absorption spectrum of two Type Ib samples one with O_2 impurities and other with N impurities [66], the absorption coefficient is measured as < 1cm^{-1} for the diamond sample with N impurities, that is > 10 ppm. The comparison of the two Type Ib diamond samples with different N impurity yields the importance of concentration of the impurities on the absorption coefficient.

3.3 Electron Transitions and Corresponding Emissions

Diamond has unique energy transitions due to NV centers. Electronic energy transitions can be altered depending on the charge state of the vacancy site. These energy transitions yields photoluminescence (PL) caused by NV centers at different wavelengths, along with the Raman scattering caused by the molecular vibrations.

3.3.1 Raman Scattering

Raman scattering is a form of inelastic scattering, which is an outcome of the interaction of incident photons with the vibrational modes of phonons inside a molecule [67]. The resultant scattered photon has energy equal to the lost energy of the incident photon by the vibrational energy, thus has less energy or larger wavelength. Raman spectrometry will yield satellite lines below the Rayleigh scattering peak at the wavelength of the incident photon. Fig. 3.2 illustrates the energy transitions from vibrational states to virtual states. Incident photons with $h\nu_0$ energy excite the electrons at the ground state to a virtual state. If

the electron returns the ground state, then the emitted photon will have $h\nu_0$ energy, namely Rayleigh scattering.

However, Stokes Raman scattering can be achieved, if the electrons return to a vibrational state, by emitting photons with $h\nu_0 - h\nu_{vib}$, where ν_{vib} represents the vibrational frequency. An extraordinary emission, the anti-Stokes Raman scattering is also shown in Fig. 3.2. Such a phenomenon occurs, if the excitation photons excite electrons at the non-ground vibrational levels to an excited virtual state. The radiated light will have more energy, and shorter wavelength than the excitation light in such an inelastic scattering. Finally, IR absorption in between the vibrational states is shown in the figure.

Wavelength of the inelastically scattered photon of a Stokes Raman scattering as shown in Fig. 3.2 can be calculated by [68]:

$$\bar{\nu} = \frac{1}{\lambda_{incident}} - \frac{1}{\lambda_{scattered}} \quad (3.1),$$

where $\bar{\nu}$ is the Raman shift in wavenumbers (cm^{-1}), $\lambda_{incident}$ the incident photon wavelength, and $\lambda_{scattered}$ the wavelength of the scattered Stokes Raman photon.

$\bar{\nu}$ is a unique value, i.e., chemical fingerprint, for every material at a given temperature and independent of the wavelength of the excitation beam. The most typical bonding inside a diamond sample is C-C bonds, which determine the Raman shift value. The first order Raman peak of a diamond sample was previously measured to be at 1332.5 cm^{-1}, while the second order Raman was observed at 2050 - 2770 cm^{-1} with a central peak at 2450 cm^{-1} in room temperature [69].

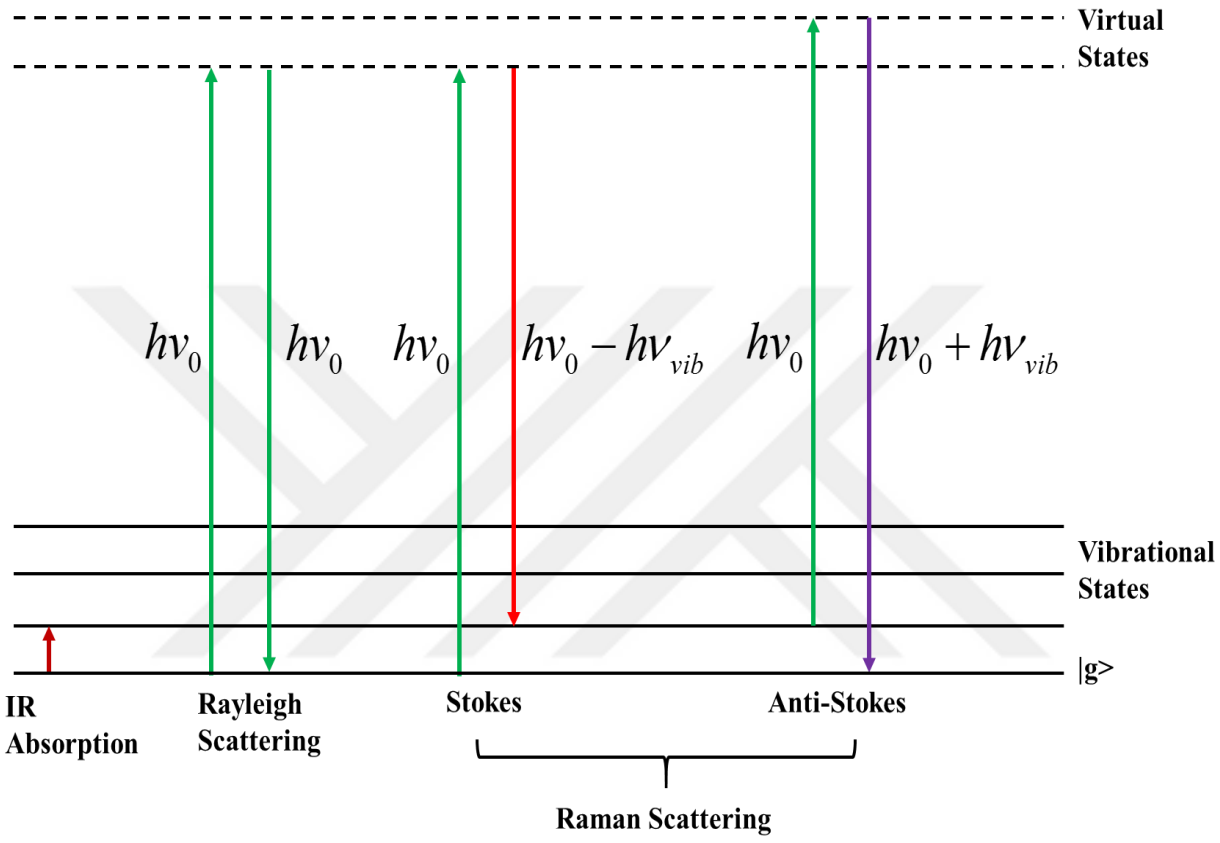

Fig. 3.2 A scheme of energy transitions for IR absorption, Rayleigh scattering, Stokes and anti-Stokes Raman scattering from real vibrational states to virtual states.

In this thesis, two excitation wavelength regions, visible and near-IR were investigated. 532 nm was the visible source, whereas the near-IR source was centered at 1427 nm. Since Stokes Raman scattering is wavelength dependent, two Raman peaks were calculated for diamond samples and tabulated in Table 3.3.

Table 3.3. Calculated 1st and 2nd Order Stokes Raman Peak Wavelengths.

$\lambda_{incident}$ (nm)	Raman Shift (cm^{-1})	$\lambda_{scattered}$ (nm)	Raman order
532	1332.5	572.6	1st
532	2450	611.7	2nd
532	1443.5	576.2	1st (sp2)
1427	1332.5	1762.1	1st
1427	2450	2194.1	2nd
1427	1443.5	1797.2	1st (sp2)

In the visible regime under 532 nm green excitation, 572.6 nm and 611.7 nm peaks are expected to be due to Raman scattering. 611.7 nm emission is dependent on the intensity of the 1st order Raman scattering, hence can be observed via Raman spectroscopy depending on the excitation intensity. Similarly, near-IR yields Raman scattering at 1762.1 nm and 2194.1 nm, however these peaks exceeds the range of the InGaAs photodetectors.

3.3.2 Photoluminescence due to NV^0 center

The two ZPL emissions from NV^0 and NV^- are at 575 nm and 637 nm, respectively. The detection of these peaks will provide the information, which is required to characterize the type of the defect in the diamond lattice. To do so, Photoluminescence (PL) spectroscopy is performed. Photoluminescence is a type of fluorescence, which is started by photoexcitation. The light with certain energy (shorter wavelength than the emission) excites an electron in the ground state to excited states. After a certain loss

to the vibrational levels, or a non-radiative relaxation, electron in these high energy states drops back to the ground state. The difference between these two energy levels results in the emission of photon (longer wavelength than the input excitation) with the same energy as the energy gap between the two transition states [70].

NV centers occur by substituting two adjacent carbon atoms by an N atom and a vacancy. The electronic structure of a vacancy site is built from three carbon dangling bond electrons, along with two electrons from the N lone pair orbital for the neutral charge state, namely NV^0 [71]. These impurities can occur naturally, or by N-ion implantation. The atomic structure of an NV^0 center is illustrated in Fig. 3.3.

It is very challenging to achieve stable NV^0 centers, while photoionization induces a transition in between $NV^0 \leftrightarrow NV^-$ [72]. Both of these impurities exhibit zero phonon line (ZPL) emissions in different wavelengths along with corresponding possible phonon side bands (PSB) under photoexcitation at proper wavelengths. A ZPL occurs, if the emission is solely due to the electronic energy transitions and a PSB follows ZPL emission [73]. The detection of the ZPL emissions in photoluminescence (PL) spectroscopy can relate the emission to a certain point defect, and we used this approach to identify the impurities in the diamond lattice.

As is previously mentioned, diamond has unique optical properties. The electronic bandgap of diamond (energy difference between the valance band and conduction band) is 5.5 eV, that corresponds to 225 nm UV radiation, which is relatively high compared to the other elements such as Si, that is 1.12 eV [74]. The NV centers induce changes in the energy levels, and the resultant electron transitions change accordingly. The energy transition of an electron from ground state to an excited state by a 532 nm photon at an NV^0 center is shown in Fig. 3.4 [75].

NV^0 center can be excited by a 532 nm green laser source to observe the ZPL emission. The energy difference between the ground state and the excited state is 2.156 eV, which corresponds to 575 nm photon irradiation. Following the 532 nm excitation, first, a non-radiative relaxation to ^2A state from an arbitrary virtual state, then a radiative relaxation to ^2E ground level occurs at the NV^0 center. Furthermore, a non-radiative two-level transition from excited state to singlet state, namely $^4A_2$, also occurs at the point defect. By performing a PL spectroscopy, the 575 nm emission can be detected at room temperature.

Again, the photoexcitation will alter the charge of an NV center by the photoionization process, and the resultant NV^- center will exhibit a different electronic energy transition.

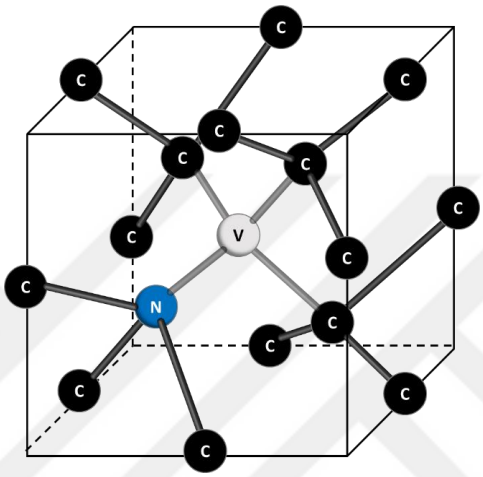

Fig. 3.3 Atomic structure of a NV^0 center implanted in diamond carbon lattice.

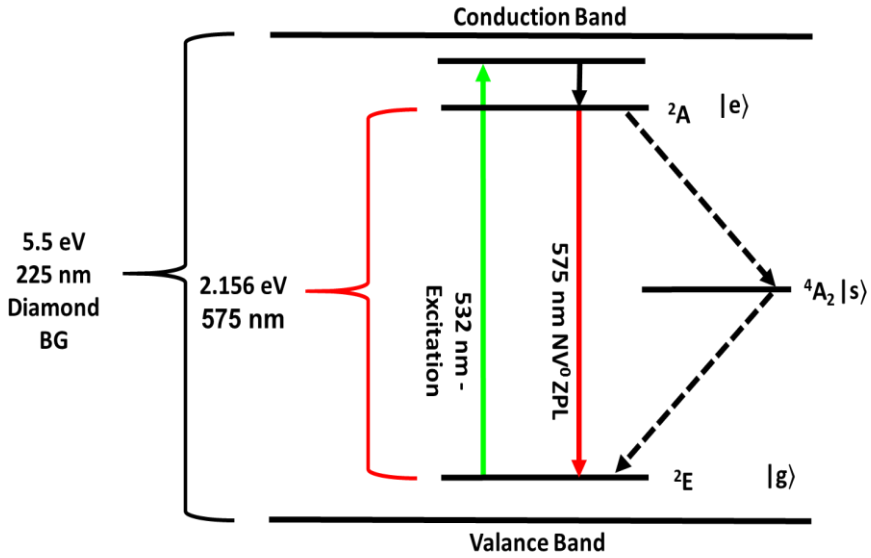

Fig. 3.4 Electronic energy transition diagram of a NV^0 center.

3.3.3 Photoluminescence due to NV^- center

The negative charge state of a NV site is called the NV^- center. The atomic structure of the charged vacancy is given in Fig. 3.5 [76]. NV^- has 1 extra electron located at the vacancy site forming an S=1 spin pair, represented with e- in the figure. This extra electron vacancy center is optically addressable and has long-lived electronic spin state compared to the neutral site [72].

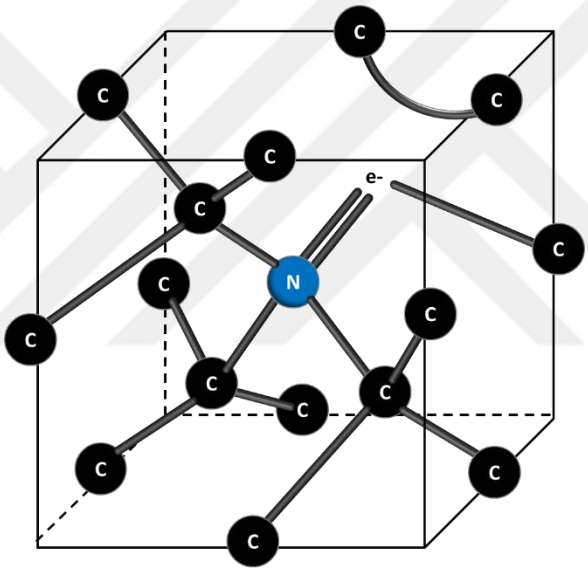

Fig. 3.5 Atomic structure of a NV^- center implanted in diamond carbon lattice.

Spin state of the excess charge at this vacancy site can be controlled with the interaction of the electron with a photon, thus gives rise to applications in quantum information processing [15]. The energy levels and the energy transitions of excited electrons of the NV^- center are illustrated at Fig. 3.6 [77]. ZPL emission of NV^0 center was previously discussed to be at 575 nm, while NV^- emission is observed at 637 nm at room temperature for diamond samples.

Here, the excitation is again performed by a 532 nm light source. Due to the excess electron, there are two additional spin states, $m_s \pm 1$, in both excited energy level, ^3E, and ground state, $^3A_2$. The allowed transitions, that yields photon emission is from |0> at excited state to |0> at ground state, and |-1> excited

state to |+1> ground state. Both of these emissions are at 637 nm, and this is the ZPL emission caused by the NV^- center [78]. Besides, there is a strong and weak non-radiative relaxation to the $^1A_1$ singlet state, and the electron transition to ^1E singlet state from the weak relaxation yields photons with a wavelength of 1042 nm, but strong non-radiative relaxation does not emit photons.

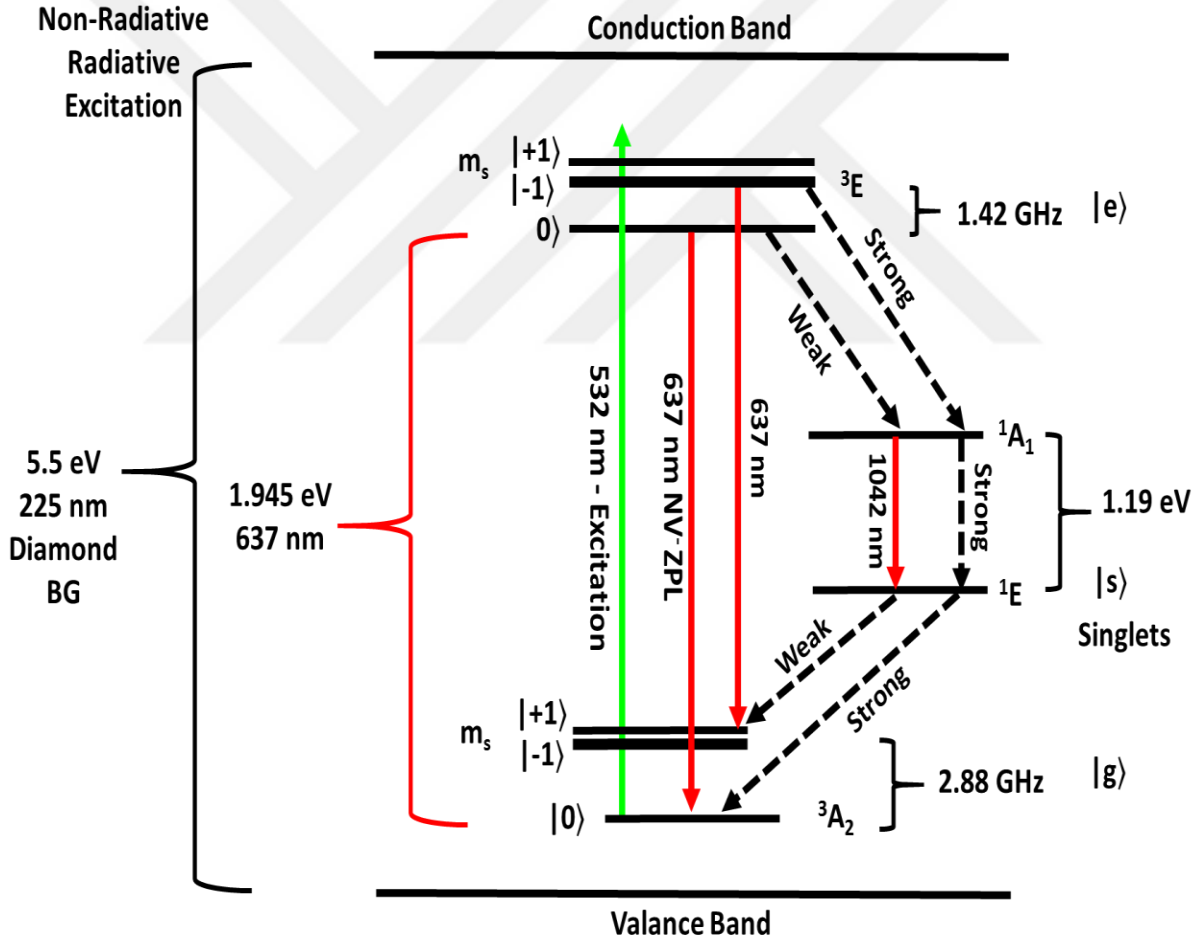

Fig. 3.6 Electronic energy transition diagram of a NV^- center.

Chapter 4

SPECTROSCOPY OF DIAMOND

4.1 Diamond Samples

Raman and photoluminescence spectroscopies are performed for various diamond samples in order to characterize the optical properties of diamond in detail. The samples are categorized in two groups as bulk diamond samples and spherical diamond, and spectroscopy of these samples are studied in this chapter.

4.1.1 Bulk Diamond Samples

Total of 18 bulk diamond samples were investigated for spectroscopic purposes. These samples are separated into three groups, namely D1-6, Dn1-6, and Dn7-12. The bulk diamond samples are numbered with respect to their sizes. The diameters, *D*, of these samples (diameter of the bulk diamond at its largest possible great circle) were measured by a Mitutoyo Digital micrometer [79]. Most of the samples have special jewel cuts, i.e., round brilliant, princess, and radiant, so that, they possess a measureable diameter. The measureable diameter is located at the top flat portion of the sample as shown in Fig. 4.1, which represents a schematic of a bulk diamond sample.

The 18 samples are tabulated as shown in Table 4.1 with their corresponding *D*, and a given color code. The color codes of the samples are identical for each group, and are in a descending order starting from the largest sample as black, red, green, yellow, blue, and violet. These color codes will be further used in the Raman and PL spectra to identify the corresponding diamond sample at the given group to prevent any confusion in the data.

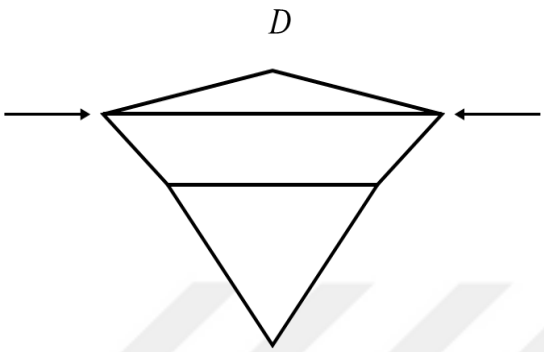

Fig. 4.1 Schematic of a bulk diamond sample with an arbitrary jewel cut.

Table 4.1. Groups, Color Codes and Diameters of Bulk Diamond Samples

Group 1		Group 2		Group 3	
Color & Code	***D* (mm)**	**Color & Code**	***D* (mm)**	**Color & Code**	***D* (mm)**
D1	1.910	Dn1	2.047	Dn7	1.915
D2	1.799	Dn2	1.849	Dn8	1.762
D3	1.414	Dn3	1.395	Dn9	1.419
D4	1.296	Dn4	1.363	Dn10	1.354
D5	1.293	Dn5	1.339	Dn11	1.318
D6	0.693	Dn6	1.315	Dn12	1.283

The samples are purchased from a jewel wholesaler, except D6, which was synthetically grown in a laboratory environment via CVD technique by Dutch Diamond Technologies [80]. The rest of the samples are confirmed to be Type Ia natural diamond samples with nitrogen as their main impurity and D6 is classified as Type Ib. The difference between these two types are due to the structure of present N atoms, i.e., N clusters vs. single N atoms as defined in the previous chapter.

Images of the first group bulk diamond samples acquired by a microscopy imaging system are shown in Fig. 4.2. As is seen in the figure, D1 to D5 samples are natural types with different forms of jewel cuts, while D6 is a synthetically grown diamond. Colors of the samples differ with respect to the amount of N impurities inside the diamond like carbon lattice.

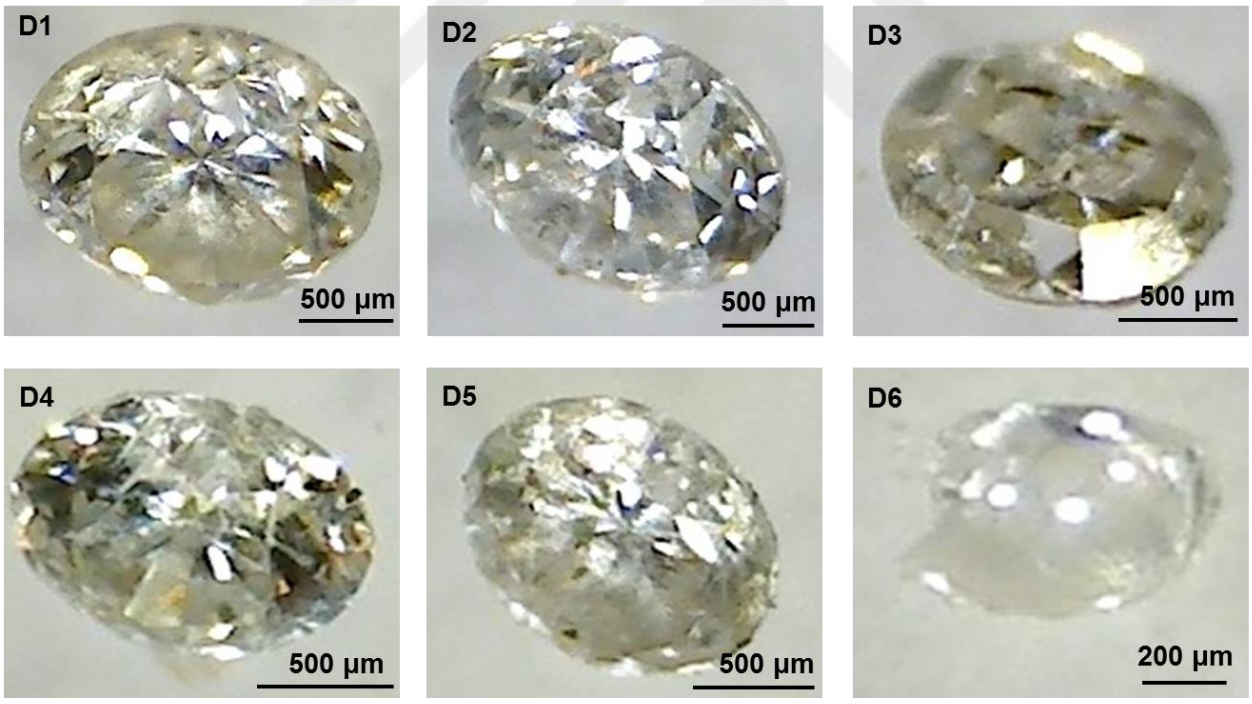

Fig. 4.2 Microscopic images of group 1 bulk diamond samples.

4.1.2 Diamond Microsphere

The diamond microsphere is grown and shaped by Dutch Diamond Technologies [80]. Fig. 4.3 shows the image of the 500 μm radius monocrystalline diamond microsphere acquired by a visible camera. The diamond sample is synthetically grown by chemical vapor deposition (CVD). Spherical geometry of the diamond is achieved by a specialized lapping machinery with a roundness defined by its form accuracy < 250 nm. The surface of the sample is polished to minimize the surface roughness, and to realize the required smooth surface finish for the WGMs. The nitrogen impurity of the microsphere is > 5 ppm, thus classified as Type Ib, which indicates the existence of NV centers as discrete point defects in the lattice.

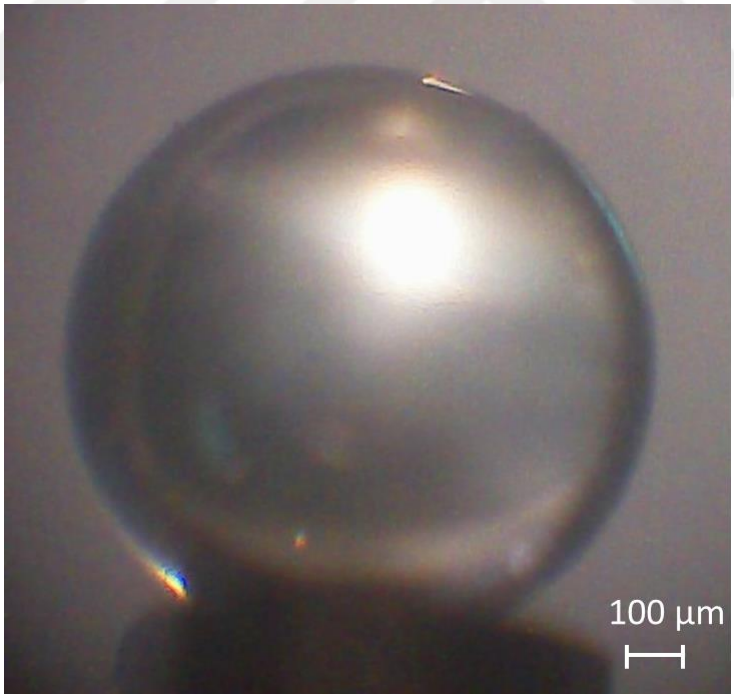

Fig. 4.3 The image of diamond microsphere held by a needle tip acquired by a visible camera.

4.2 Raman Spectroscopy of Diamond

Raman spectroscopy is performed with the diamond samples, which are tabulated in Table 4.1 to measure the corresponding Raman shifts due to the vibrational modes of diamond. Previous measurements indicate the shift as 1332.5 cm^{-1}, while the second order Raman was observed at 2050 - 2770 cm^{-1} with a central peak at 2450 cm^{-1} in room temperature [69].

4.2.1 Experimental Raman Spectroscopy Setup

In order to detect the Raman emissions, the experiment is performed by using the Renishaw inVia Raman Microscope and the apparatus is shown in Fig. 4.4 [81]. The excitation source is a 532 nm continuous wave (CW) diode pumped solid state green laser with a maximum power of 60 mW. The spectrometer is built-in, and the gratings allow to scan the range between 500 nm – 780 nm, which falls into the desired range of the electromagnetic spectrum for Raman shift measurements.

After calibration, %1 of the maximum laser power is used to excite the electrons with 2 μm spot size using 50x objective to focus the laser beam on the center of the diamond samples. Excitation of the sample and collection of the scattered and/or luminescing light are achieved from the aperture of the same microscope objective. Then, the data acquisition (DAQ) is performed in the range between 550 nm to 680 nm, to prevent the detection of 532 nm source, which will saturate the photodetector. A solid state detector is also used, converting the light signal into an electrical signal, thus yielding the microRaman spectra for the diamond samples.

This instrument can also be used to measure PL spectra, which will be discussed in the next sections. Similarly, the Raman scattering emission will be indicated on the corresponding PL spectra.

Fig. 4.4 Renishaw inVia Micro Raman Microscope System.

4.2.2 Raman Spectra of Diamond

Raman spectroscopy is performed for Group 2 and Group 3 diamond samples with 532 nm excitation source. The spectral range is from 150 cm^{-1} to 1750 cm^{-1} with a step size of 1 cm^{-1}. 1% of the maximum laser power is used with a 50x focusing lens, and the samples are targeted at their central location with respect to their top view.

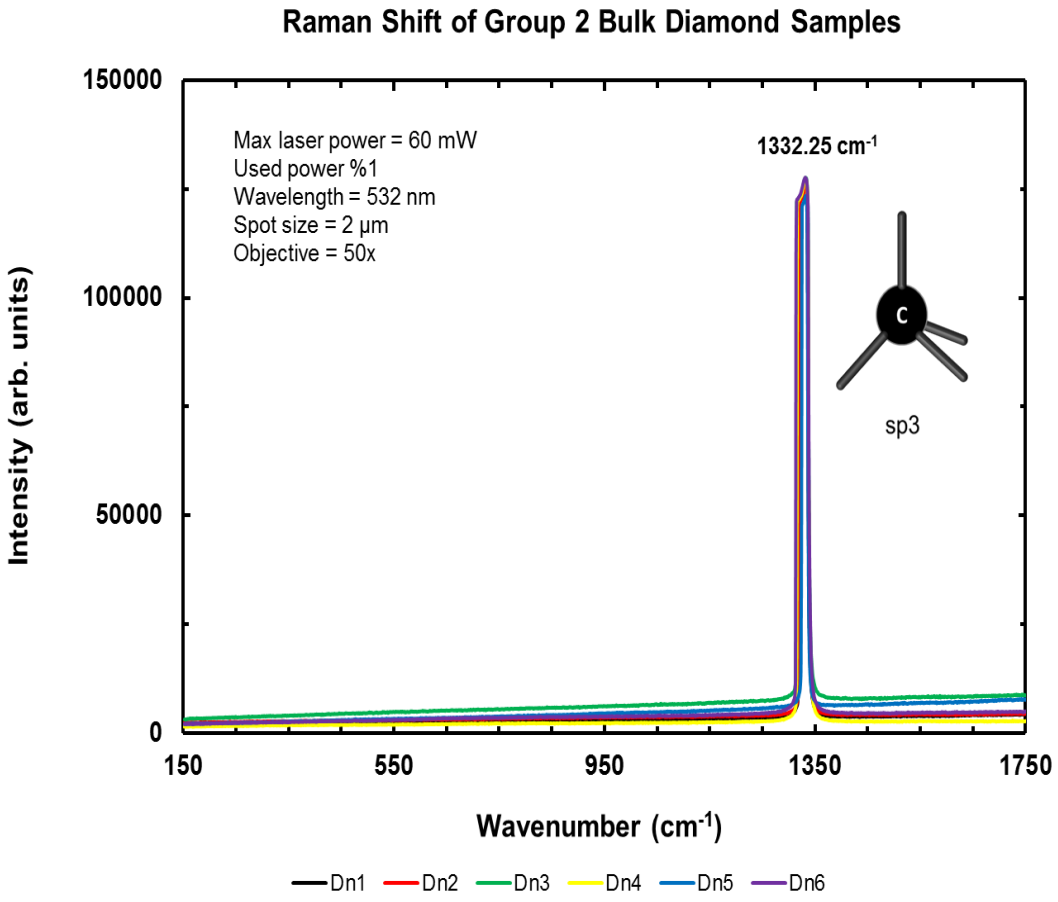

Fig. 4.5 Raman scattering spectra of Group 2 bulk diamond samples.

Fig. 4.5 shows the Raman spectra of group 2 diamond samples with the given color codes as formerly presented in Table 4.1. The shifts are measured to be 1332.25 cm^{-1} for each diamond sample, which are in a great correlation with the previously measured values [69]. 1332.25 cm^{-1} denotes the sp^3 configuration of the C-C bonding inside the diamond carbon lattice [82]. However, C atoms can also form sp^2 configuration by replacing two of the four tetrahedral bonds with a double bond, which will alter the angles between the bonds. Therefore a different emission can be achieved with the change in the

vibrational directions due to a change in the angles. Such a phenomenon is observed in the group 3 diamond samples.

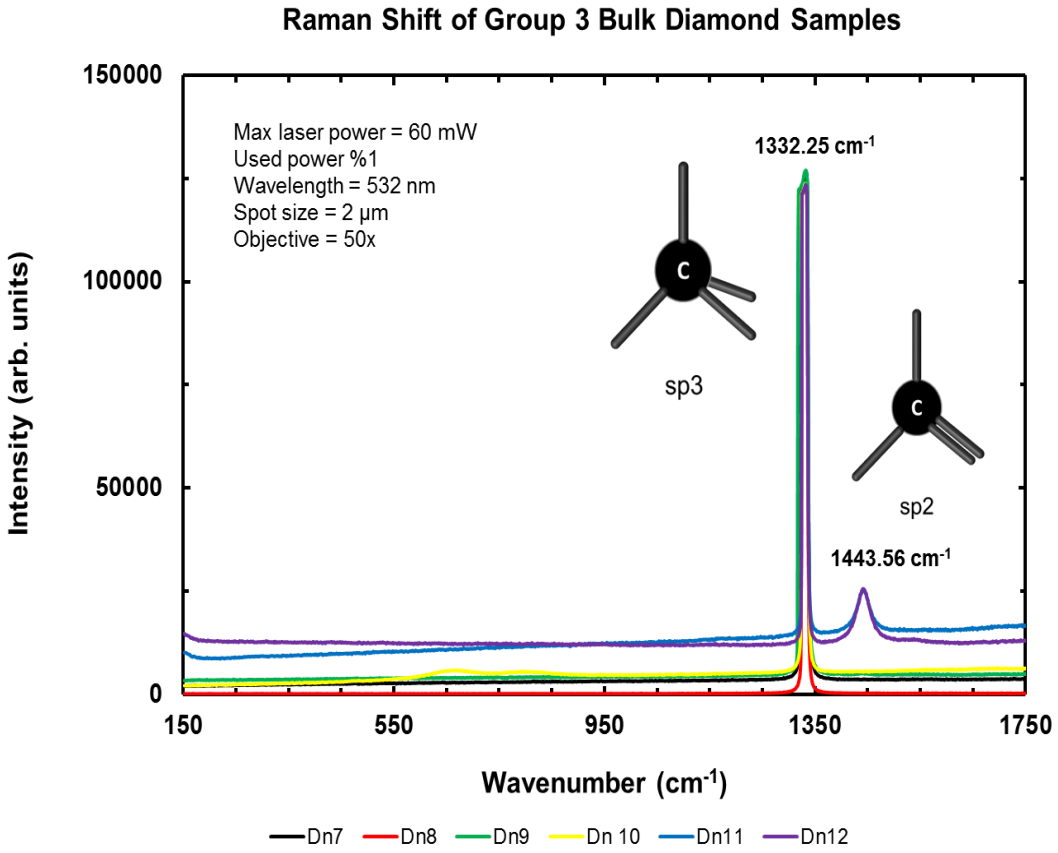

Fig. 4.6 Raman scattering spectra of Group 3 bulk diamond samples.

Raman spectra of group 3 bulk diamond samples are given in Fig. 4.6. In contrast to Fig. 4.5, there is an extra signal observed at ≈ 1444 cm^{-1}. This emission is measured only for Dn11 and Dn12. Previously, a similar peak is identified as a result of sp^2 configured C-C bonding [83]. Therefore, it is clear that, Dn11 and Dn12 has sp^2 bonding within the diamond lattice.

It is possible to calculate the wavelengths of the following emissions, that are shown in both Fig. 4.5 and Fig. 4.6 by using Eq. (3.1). 1332.25 cm^{-1} Raman shift, yielding an inelastically scattered photon with a wavelength of 572.6 nm, is again due to the incident photon at 532 nm. Similarly, 1444 cm^{-1} shifts the wavelength of the incident beam to 576.3 nm. These peaks can be seen on the PL spectra of these samples, as well.

Additionally, the Raman scattering of the diamond microsphere will be shown on the PL spectrum in the next section.

4.3 Photoluminescence Spectroscopy

Photoluminescence (PL) spectroscopy is performed with the diamond samples in order to observe and identify the cause of the fluorescent peaks. PL measurements for the samples shown in Table 4.1 are performed with the inVia Renishaw Raman Microscopy System, which is given in Fig. 4.4. However, a different measurement setup is used to measure the PL of the diamond microsphere, due its unique morphology, which will be described further in the following sections.

4.3.1 PL of Diamond Samples by the MicroRaman Microscope

PL results acquired from the group 1 diamond by the microRaman Microscope is illustrated in Fig. 4.7. 1% of a 60 mW 532 nm CW laser is used to excite the diamond samples targeting the center of each sample for a spectral range of 540 – 690 nm. As mentioned before, D6 is a synthetic Type Ib diamond, while the rest of the samples are natural Type Ia. D1, D3 and D6 are shown on the primary axis (left), and D2, D5 and D6 on the secondary axis (right), since the photon count of the first three samples are greater that of the last three, which are also indicated with the arrows on the graph with their corresponding colors.

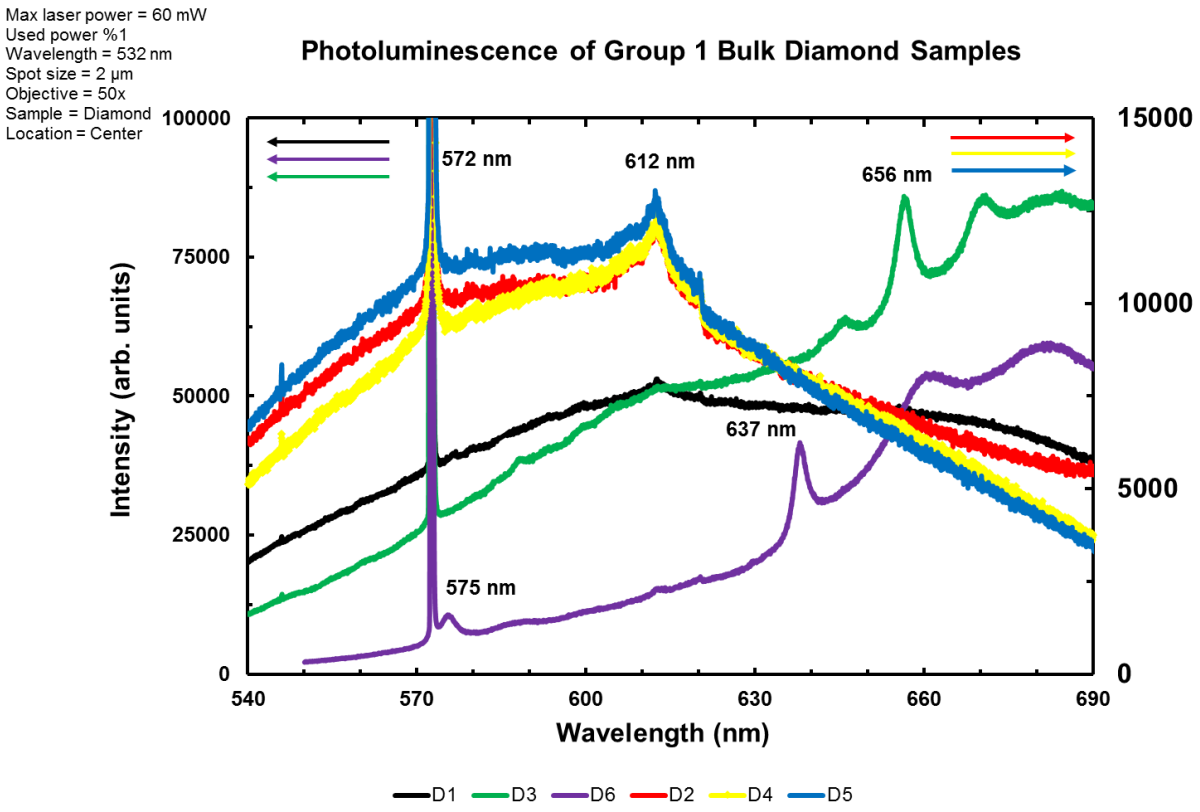

Fig. 4.7 Group 1 bulk diamond samples PL spectra by inVia Renishaw RamanMicroscope System.

Five significant peaks are observed at Fig. 4.7. The 572 nm peaks are acquired for all group 1 samples, which also represent the Raman scattered photons from the diamond samples. C-C bonds of sp^3 configuration has a Raman shift of 1332.25 cm^{-1}, and yields 572 nm scattered light for 532 nm incident photons, as shown in Fig. 4.5 and Fig. 4.6. The next peak is at 575 nm, which exhibits itself only at D6, and is the PL due to NV^0 center as given in Fig. 3.4. The 612 nm peak is the 2^{nd} order Raman scattering, as calculated before by using Eq. (3.1), and is observed at all group 1 bulk diamonds. The peak at 637 nm is seen in D6, and is due to the fluorescence of NV^- centers inside the diamond carbon lattice, which is represented by Fig. 3.6. Also there is a phonon side band (PSB) following the NV^- zero phonon line (ZPL) emission after 637 nm for D6. Finally, a peak at 656 nm is measured from D3, which is defined as

the center created in natural Type Ia, and common synthetic diamonds treated by neutron irradiation. The center has a relatively narrow ZPL and low-vibrational side-band [63,84].

Fig. 4.8 represents the PL spectra of group 2 bulk diamond samples, which are acquired under the same conditions with the group 1 diamond samples. Similar to the previous figure, peaks at 572 nm, 612 nm, and 656 nm are observed for most of the diamond samples, which are all Type Ia. The group 2 sample results are in a good correlation with the group 1 diamond samples.

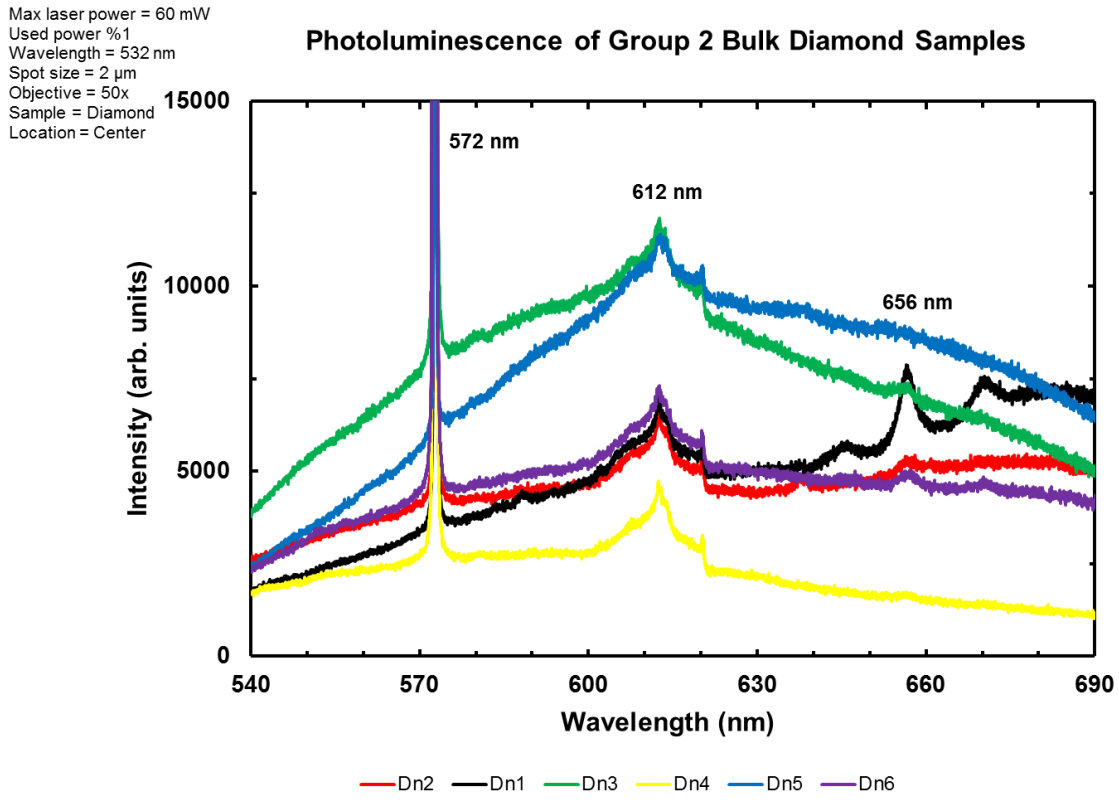

Fig. 4.8 Group 2 bulk diamond samples' PL spectra by inVia Renishaw Raman Microscope.

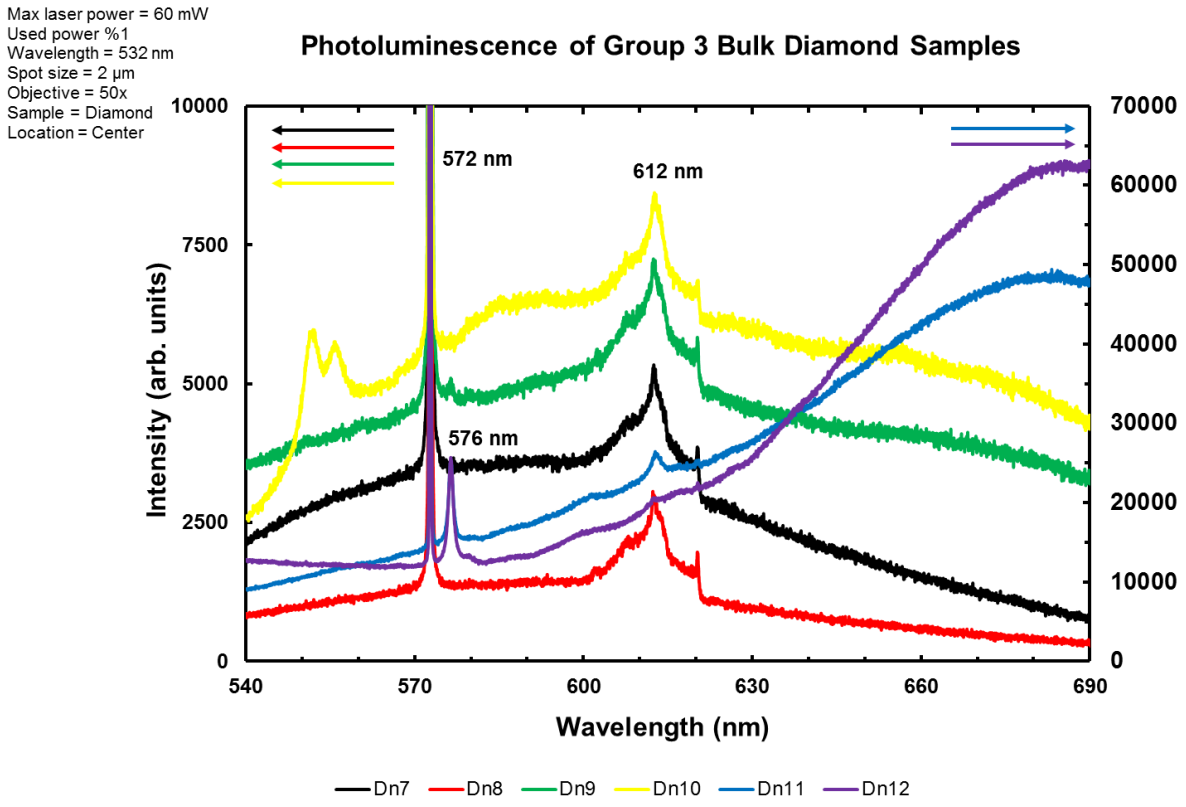

Fig. 4.9 Group 3 bulk diamond samples' PL spectra by inVia Renishaw Raman Microscope.

Group 3 bulk diamond samples PL spectra are given in Fig. 4.9. Results are similar to that of group 1 and 2. Only the 576 nm peak was not present in the previous data. This peak is the result of the 1444 cm^{-1} Raman shift obtained in Fig. 4.6 for Dn11 and Dn12, and is due to sp^2 configuration of a portion of the C-C bonds [83]. Besides, the photon count from Dn11 and Dn12 are greater compared to Dn7, Dn8, Dn9, and Dn10. Also, a strong PSB is observed between 630-690 nm for Dn11 and Dn12.

Peaks related to nitrogen impurities are only measured for D6, which is a Type Ib diamond sample. However, Raman scattered photons are measured for each of these samples. This may be related to the excitation laser power, which is around 5 mW. Therefore, different PL measurements are performed using the same samples with a more powerful laser, along with the diamond microsphere.

4.3.2 PL Spectroscopy Setup for the Diamond

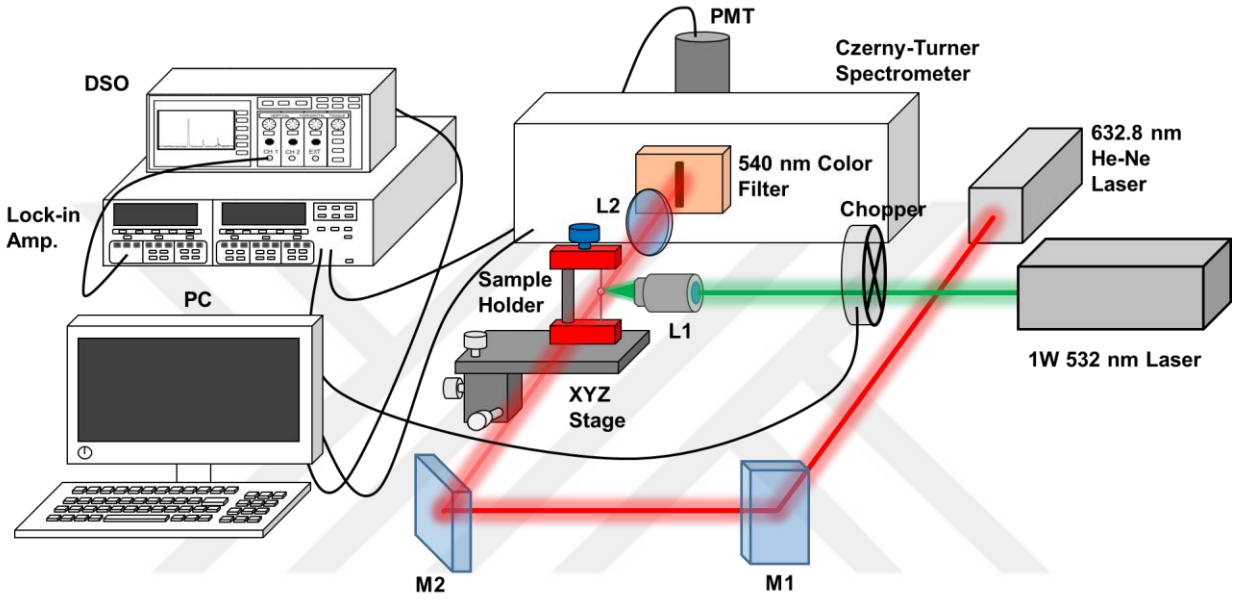

Fig. 4.10 PL spectroscopy setup of bulk diamond samples and the diamond microsphere.

The schematic of the experimental setup for PL spectroscopy is shown in Fig. 4.10 and, , its image is given in Fig. 4.11. In this setup, the excitation is performed by a 1W continuous wave (CW) mode 532 nm green single longitudinal mode (SLM) laser manufactured by Changchun New Industries Optoelectronics Tech. Co. Ltd. (CNI Lasers) [85]. The spectral linewidth of this laser is < 10 fm, and the spot size is Ø = 1.826 mm. Output of the laser is vertically polarized in TEM_{00} mode. A 632.8 nm He-Ne laser is used along with the 532 nm laser to align the optic axis together with the alignment mirrors M1 and M2, and for the calibration of the spectrometer.

A custom build diamond sphere holder is manufactured in order to stably contain the sphere during data acquisition (DAQ), and prevent any contaminations. The holder consists of two engraved needles, which are placed face to face on two movable metal tubes to squeeze the sphere between their tips. Then the needle tips and the sphere are covered with a glass capillary tube with a diameter of 2.046 mm as

shown in the image presented in Fig. 4.12. Then, the holder is anchored to a XYZ 3-dimensional translational stage with 20 mm range and 20 μm step size, to position the sphere on the optic axis with respect to the green excitation laser beam.

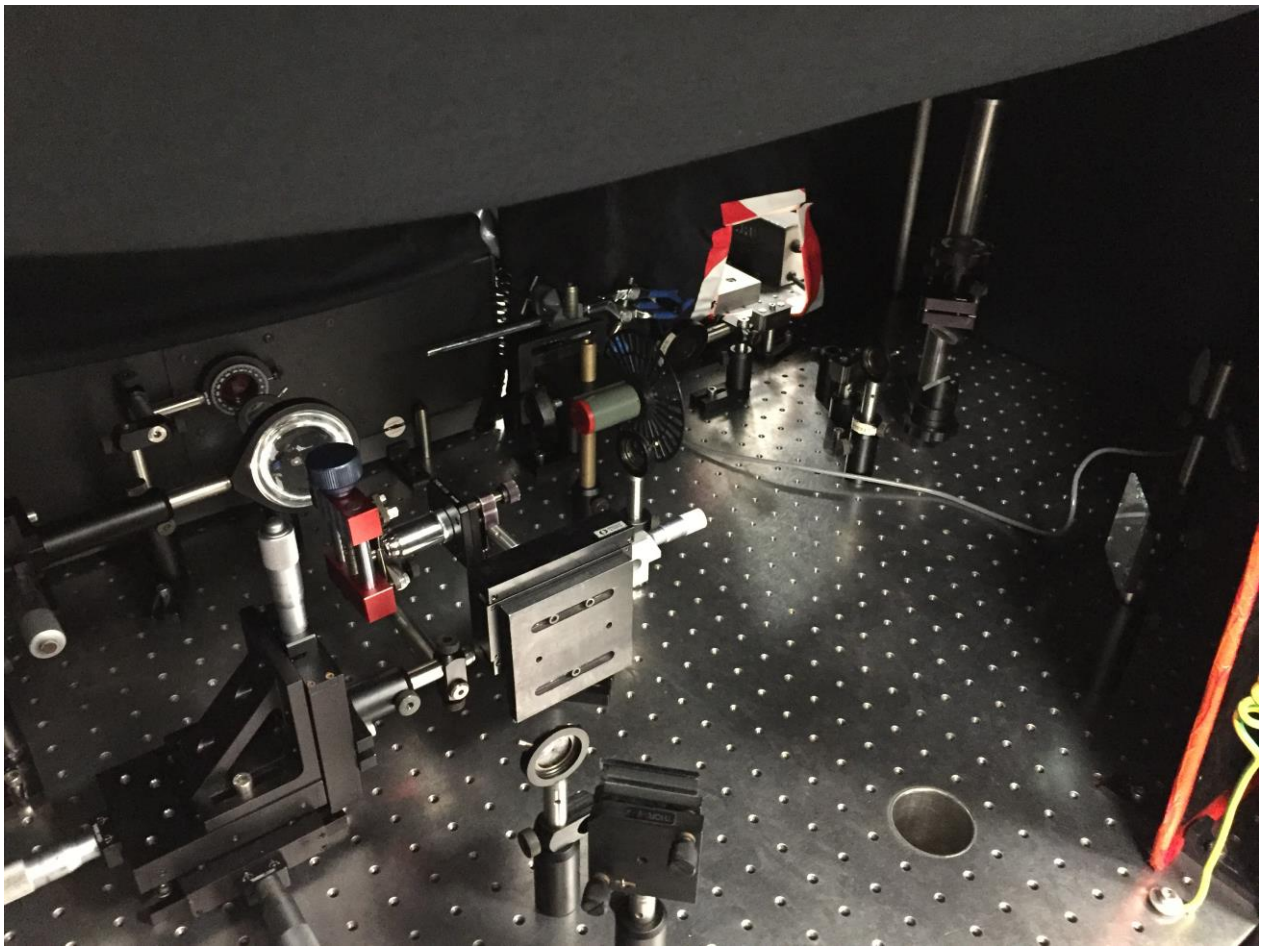

Fig. 4.11 Image of the diamond PL spectroscopy setup.

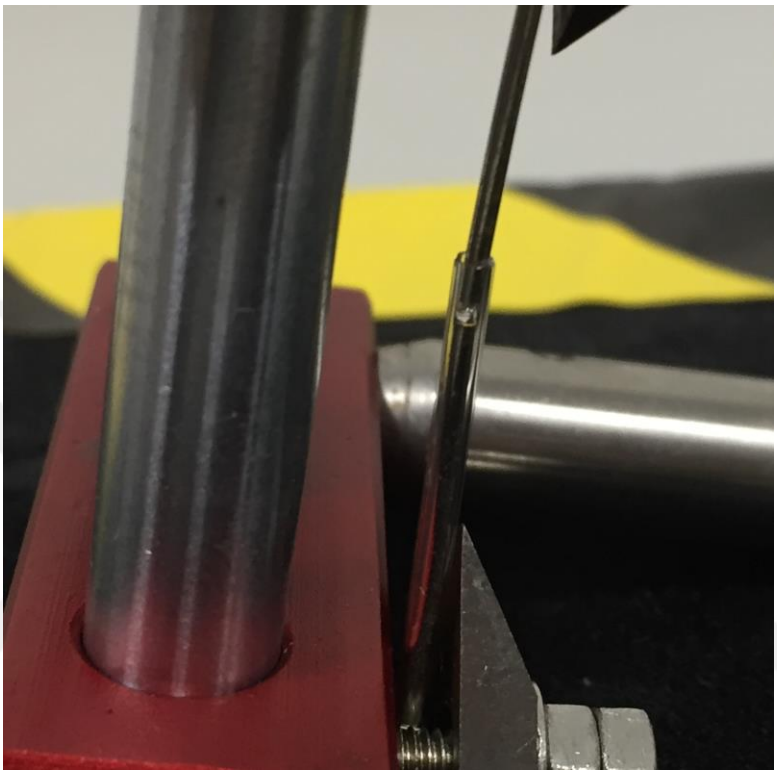

Fig. 4.12 Image of the sample holder along with the diamond microsphere, the two holding needles, and the capillary glass tube.

The 532 nm CW laser is focused on the diamond samples using a microscope objective with 20x magnification, denoted as L1 on Fig. 4.10. This objective has a numerical aperture *NA* = 0.40, a working distance WD = 1.7 mm, and the focal length f = 9.0 mm. The spot size of the focused beam is then calculated by:

$$\varnothing = 1.22 \times \frac{\lambda}{NA} \qquad (3.2),$$

where λ = 532 nm denotes the wavelength of the incident beam. The calculated focused spot size Ø is 1.622 μm.

The scattered light is collected by a collection lens L2, and focused into the entrance slit of the spectrometer. The position of L2 with respect to the entrance slit is calculated by using the lens equation. The collected light first goes through a 540 nm high pass color filter in order to prevent the 532 nm scattered light enter the spectrometer. The transmission spectrum of the used color filter between 300 - 1900 nm is shown in Fig. 4.13, which is acquired by a UV Spectrophotometer.

A Czerny-Turner spectrometer, produced by CVI, is used as a monochromator with a grating, that operates in the range of 300 - 1100 nm, with blaze wavelength of 500 nm and with a grove density of 1200 groves/mm. The spectral resolution of the spectrometer is 0.1 nm. The range of the slit size for both the entrance and the exit slits are from 50 μm up to 250 μm. The exposure time per step is selected as 500 ms to increase the signal. The average of 3 readings per step are acquired to further reduce the noise.

A photomultiplier tube (PMT) is used for optical detection and amplification, which amplifies the signal by exposing the dynodes to a potential difference of 850V. After the optical signal is converted to an electrical signal by the PMT, the signal is send to a lock-in amplifier manufactured by Stanford Research Systems [86]. The input reference of the lock-in amplifier is achieved by an optical chopper operating at 250 Hz, which is placed on the optical axis of the 532 nm excitation source in between the sample and the laser. The amplifier is automatically locked to the reference signal to clear the noise of the acquired spectra. Lock-in amplifier's parameters are 5 x 100 mV sensitivity, and 1 x 1s (12 dB) time constant.

The resultant data is then monitored by a digital storage oscilloscope (DSO) which is controlled by a controller PC. This PC also controls the position of the Czerny-Turner spectrometer. The measured intensity with the corresponding wavelength is further matched by a LabView (National Instruments) Software.

The optical table is floated by using nitrogen gas in order to prevent physical vibrations to effect the measurements. Similarly, the laboratory is darkened, and the setup is covered with black curtains to prevent any interference caused by external light sources.

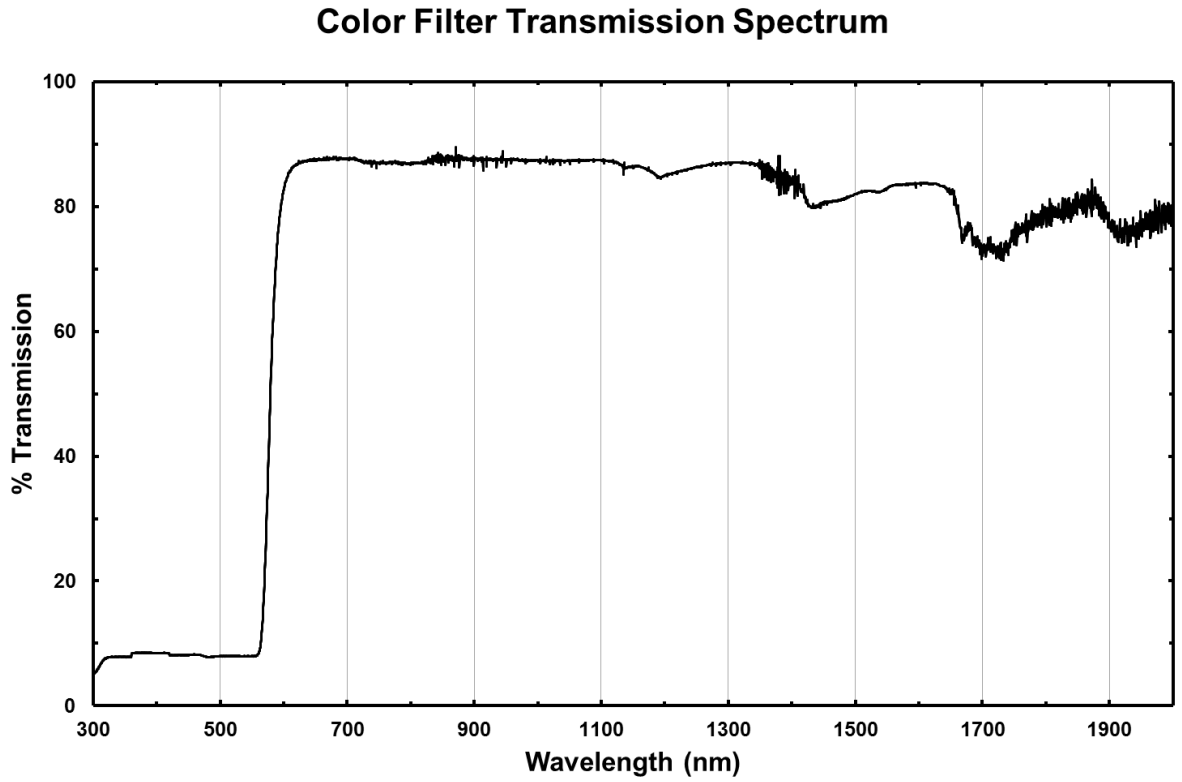

Fig. 4.13 The transmission spectrum of the color filter used in the PL measurement setup.

4.3.3 PL Spectra Acquired by the PL Spectroscopy Setup

First, the group 3 bulk diamond samples were measured using the new PL spectroscopy setup. The results are presented in Fig. 4.14. Similar results to Fig. 4.9 are achieved. However, it is possible to see the effect of N impurities in this figure. It is possible to see the 637 nm ZPL, and the corresponding PSB for the diamond samples except for Dn8. Also Dn11 and Dn12 exhibit 576 nm emission due to the sp^2 C-C configuration that, are present in the diamond lattice.

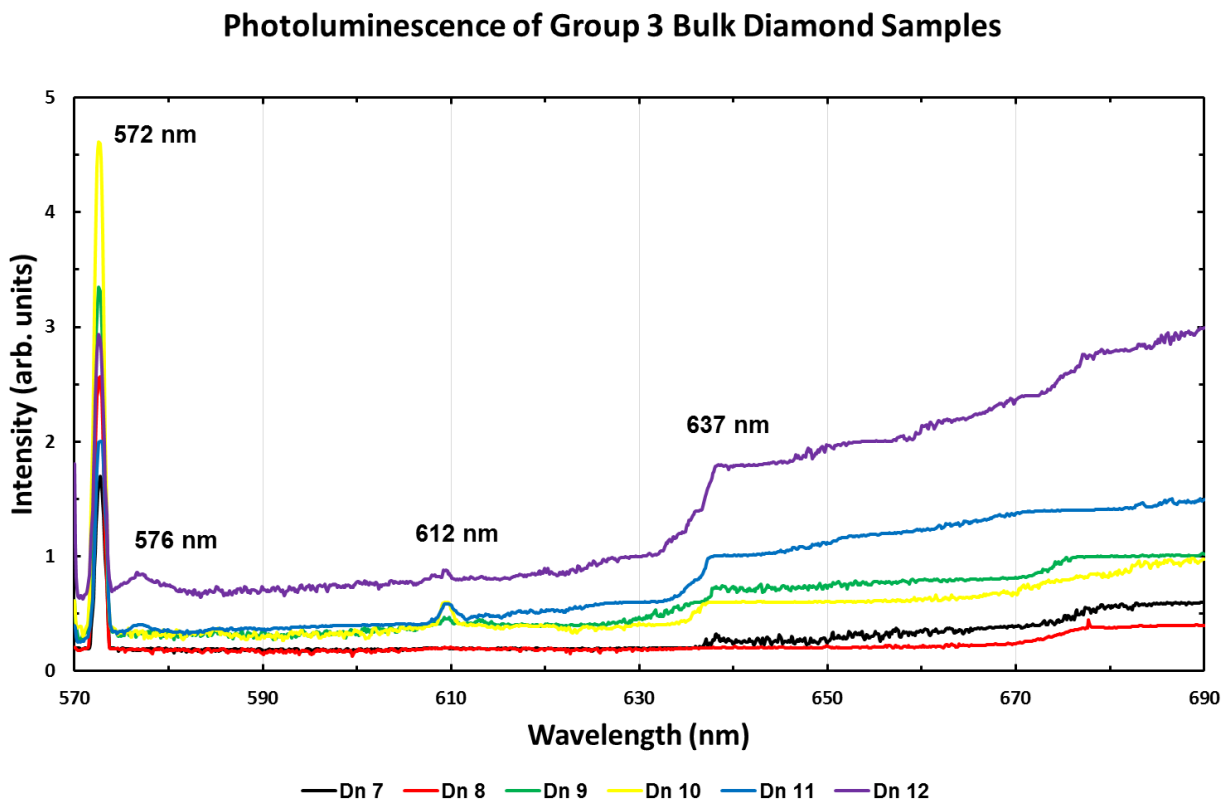

Fig. 4.14 Group 3 bulk diamond samples PL spectra acquired by the PL spectroscopy setup.

Finally, a PL measurement is performed on the diamond microsphere to observe its fluorescence properties. The measurement setup, shown in Fig. 4.10, is used to acquire the PL spectrum with the defined parameters. The image, during the excitation of diamond microsphere with the 532 nm laser, is shown in Fig. 4.15. This image is acquired by a microscope with a total magnification of 50x, and a color filter is used in front of the visible camera to block the elastic scattering from the 532 nm laser, while taking the image of the diamond microsphere.

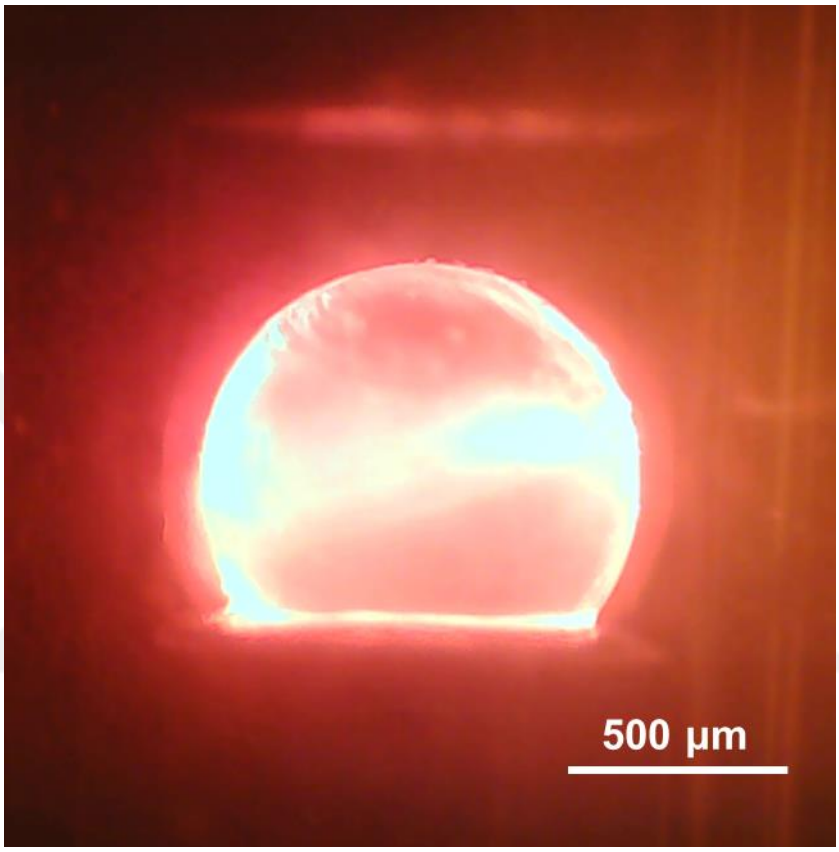

Fig. 4.15 Image of the diamond microsphere during excitation with the green 532 nm laser.

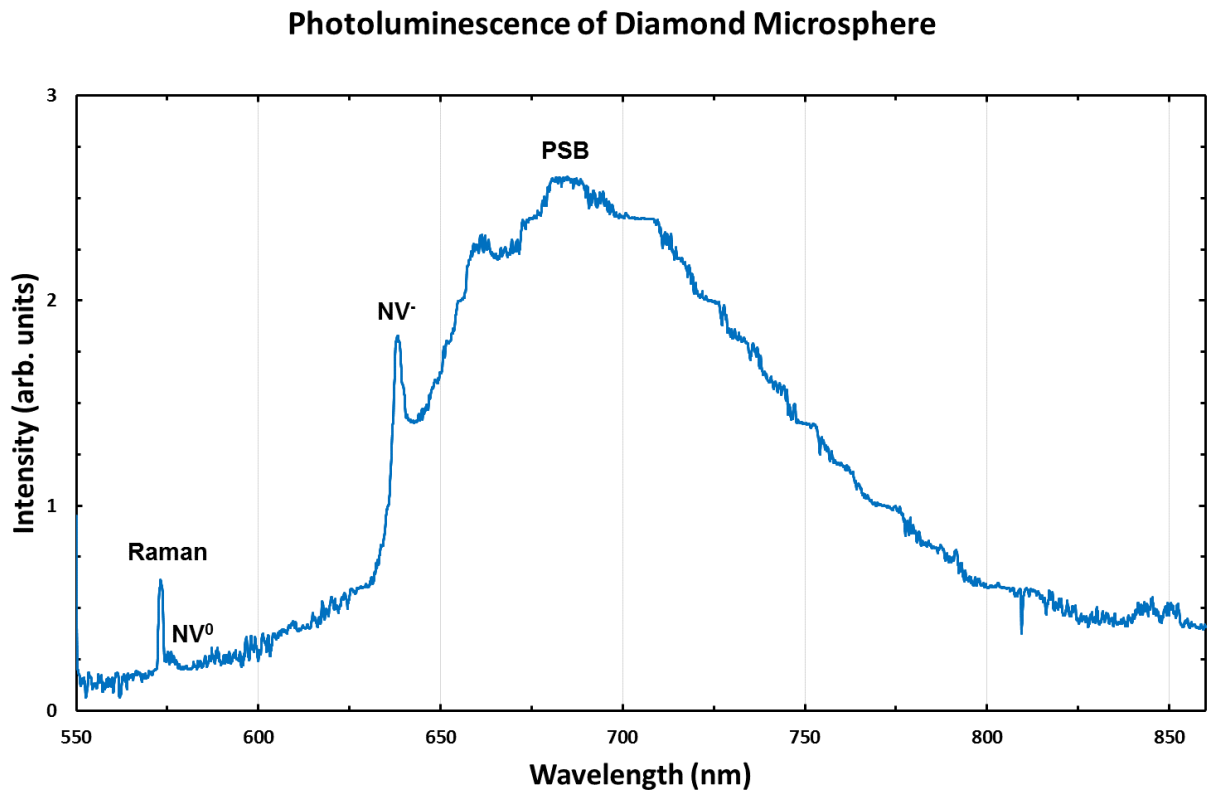

Fig. 4.16 Diamond microsphere PL spectrum acquired by the PL measurement setup.

The PL of the diamond microsphere is shown in Fig. 4.16, which is in a great correlation with the previously measured PL of Type Ib diamond samples [87]. As expected, Raman scattering is observed at 572 nm, and the emission caused by NV^0 center is observed at 575 nm. An intense ZPL of NV^- is measured along with its PSB.

These peaks prove that, the diamond microsphere is a synthetically grown Type Ib diamond with NV centers located within the diamond carbon lattice, that are not in cluster form.

Chapter 5

ELASTIC LIGHT SCATTERING OF THE DIAMOND MICROSPHERE

5.1 Elastic Scattering Spectroscopy Setup

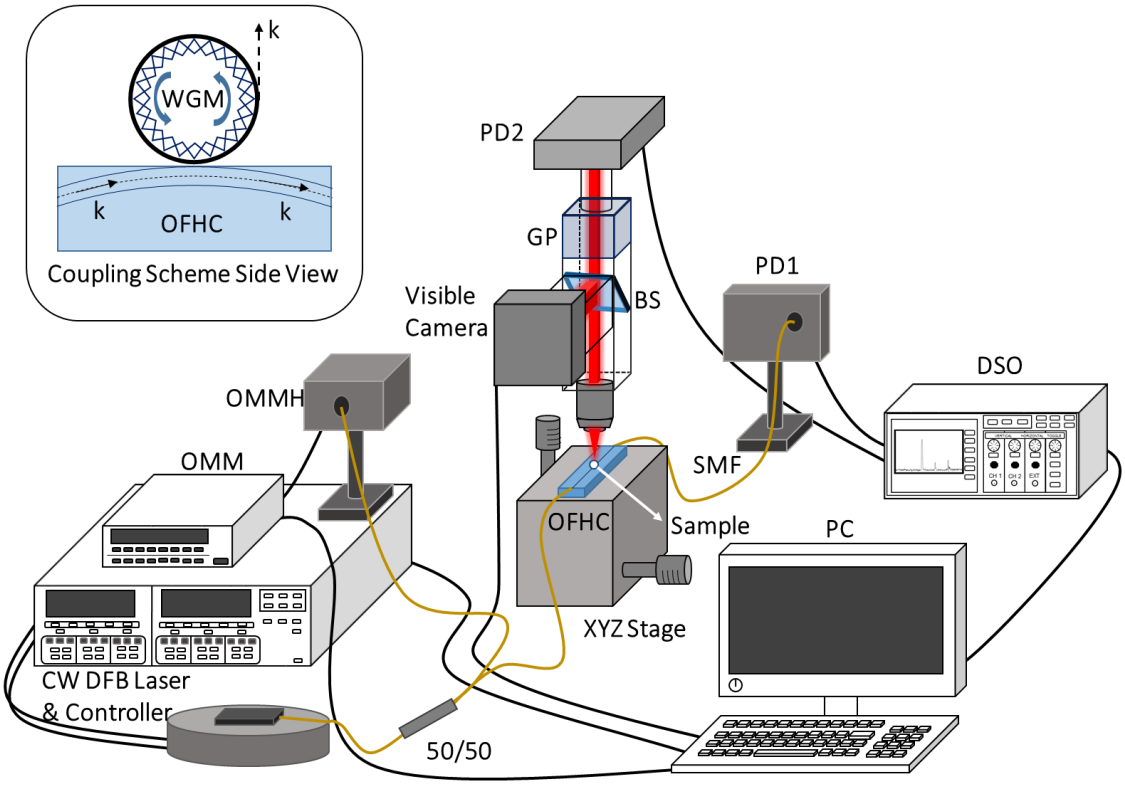

Fig. 5.1 Elastic scattering experimental setup from a diamond microsphere. The inset shows the coupling scheme to the diamond sphere in contact with optical fiber half-coupler (OFHC).

Fig. 5.1 illustrates the experimental setup used to measure the elastic scattering of the near-IR laser from the diamond microsphere. The visible images of the setup are presented in Fig. 5.2 and Fig. 5.3. An optical fiber half-coupler (OFHC), operating in the standard telecom wavelengths, is used to achieve the coupling of light from fiber to the microsphere, and is anchored on top of an XYZ translational stage with a range of 20 mm and resolution of 20 μm. The incident single mode fiber (SMF) to OFHC is connected to the pigtailed distributed feedback (DFB) diode laser, whereas the output of OFHC is connected to an InGaAs photodetector (PD1) to acquire the transmission spectrum.

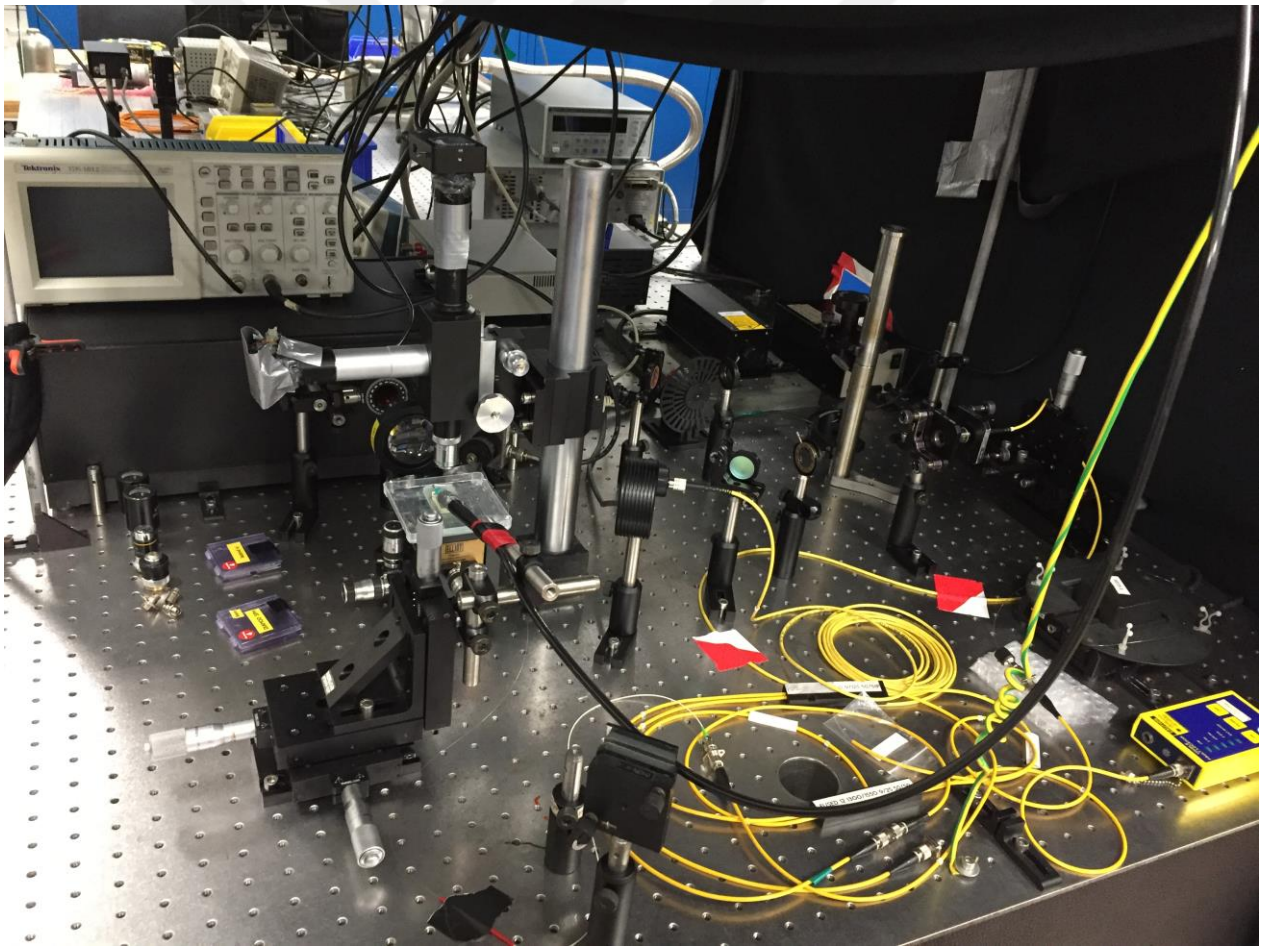

Fig. 5.2 Image of the elastic light scattering measurement setup wide view.

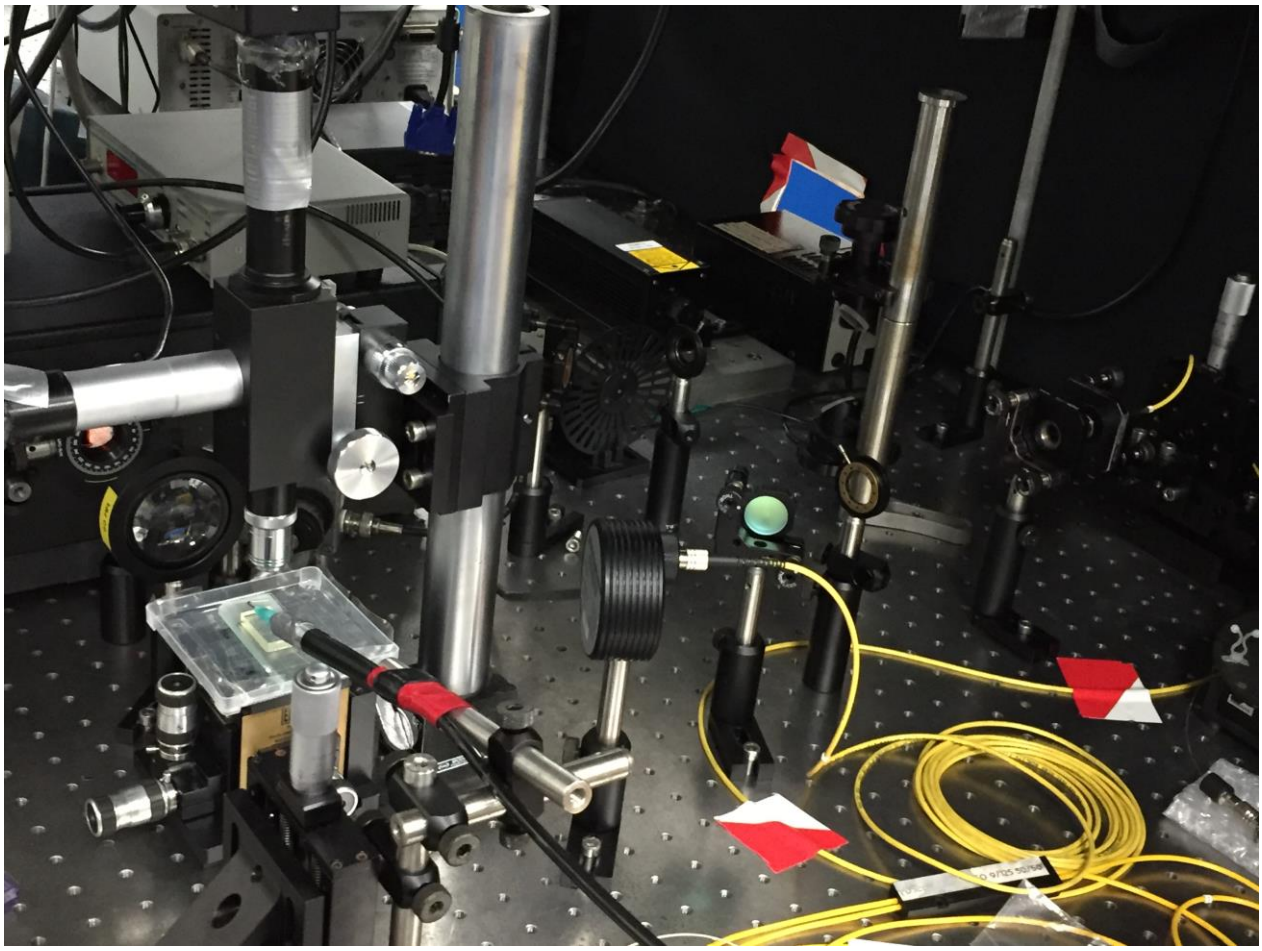

Fig. 5.3 Image of the elastic light scattering measurement setup (focusing on the OFHC).

A microscope is fixed on top of the OFHC for collection of elastically scattered light perpendicular to the transmission direction. A microscope objective with 20x magnification is used to collect the elastically scattered photons with another InGaAs photodetector (PD2) fixed on a 10x microscope eyepiece. A Glan polarizer (GP) is placed before the eyepiece to select between the transverse magnetic (TM) and transverse electric (TE) polarizations of the elastically scattered light. A beamsplitter (BS) is

placed inside the microscope to monitor the position of the diamond microsphere on top of the OFHC via a visible camera, which is attached to another 10x eyepiece.

The excitation source is a DFB semiconductor diode laser operating in continuous wave (CW) mode. DFB diode laser output wavelength control between 1426.10 nm and 1427.42 nm with a spectral resolution of 1 pm is achieved by fine tuning the laser temperature. The output optical power of the laser is monitored by an optical multimeter head (OMMH) connected to an optical multimeter (OMM).

The CW laser diode controller, the optical multimeter, and the visible camera are connected to the control computer, as well as the digital storage oscilloscope (DSO), that acquires the transmission and elastic scattering data from the photodetectors PD1 and PD2, respectively. Data acquisition is performed by LabView (National Instruments) software to construct the corresponding spectra.

A suction mechanism consists of a vacuum pump, and a thin needle tip is used to hold the sphere on the OFHC during data acquisition. The needle tip grips the microsphere from an equatorial position. The resonator is brought to the close proximity of the OFHC. The coupled light propagates around the sphere from one pole to the other. The side view of the coupling scheme of the diamond sphere in contact with the OFHC is shown in the inset of Fig. 5.1, where k denotes the propagation wavevector.

5.2 Experimental Results

5.2.1 Mode Spacing

Fig. 5.4 shows the TM polarized elastically scattered WGM resonances acquired by the diamond microsphere at 90° (blue lower curve), and transmission at 0^o (red upper curve). TM polarized 90° elastic scattering is recorded by placing the GP in parallel direction to the excitation OFHC. Four resonant peaks located at 1426.29 nm, 1426.63 nm, 1426.96 nm, and 1427.28 nm for consecutive mode families with decreasing n are indicated with the dashed lines in the Fig. 5.4. However, the corresponding resonance dips are not observable in the transmission spectrum at the resonance wavelengths. The mode spacing $\Delta\lambda_n$ is calculated as 0.340 nm for the diamond microsphere at 1426.29 nm using Eq. (2.29) by a MATLAB Script given in APPENDIX A. Experimentally, the mode spacing value is measured as 0.332 nm, which

is comparable to the calculated value. Similarly, the corresponding frequency mode spacing $\Delta\nu_n$ is 50.3 GHz.

TE polarized 90° elastic scattering is recorded by placing the GP in perpendicular direction to the excitation OFHC. Fig. 5.5 shows the TE polarized 90° elastic scattering and 0° transmission spectrum, along with the corresponding mode spacing $\Delta\lambda_n = 0.332$ nm. $\Delta\lambda_n$ for TE is comparable with the calculated and identical to the TM mode spacing.

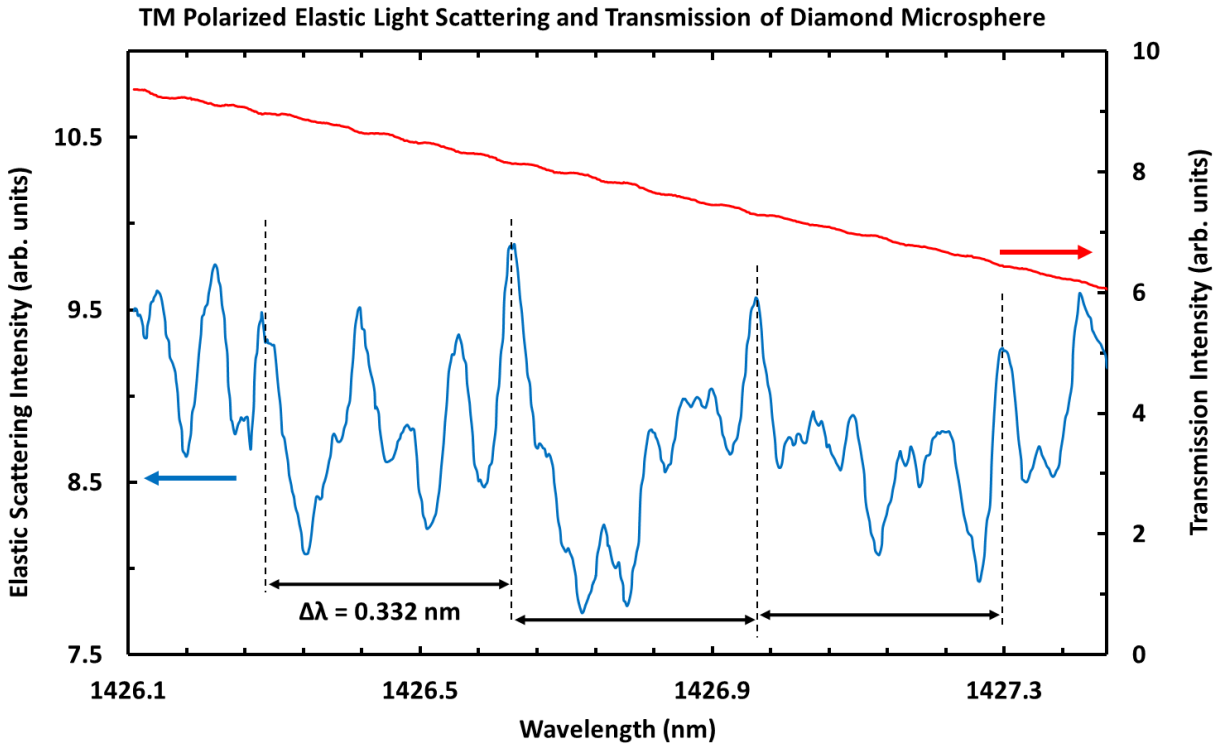

Fig. 5.4 TM polarized elastically scattering spectrum at 90° is shown in blue lower curve, and the transmission at 0° is shown in the red upper curve. The mode spacing of $\Delta\lambda_n = 0.332$ nm.

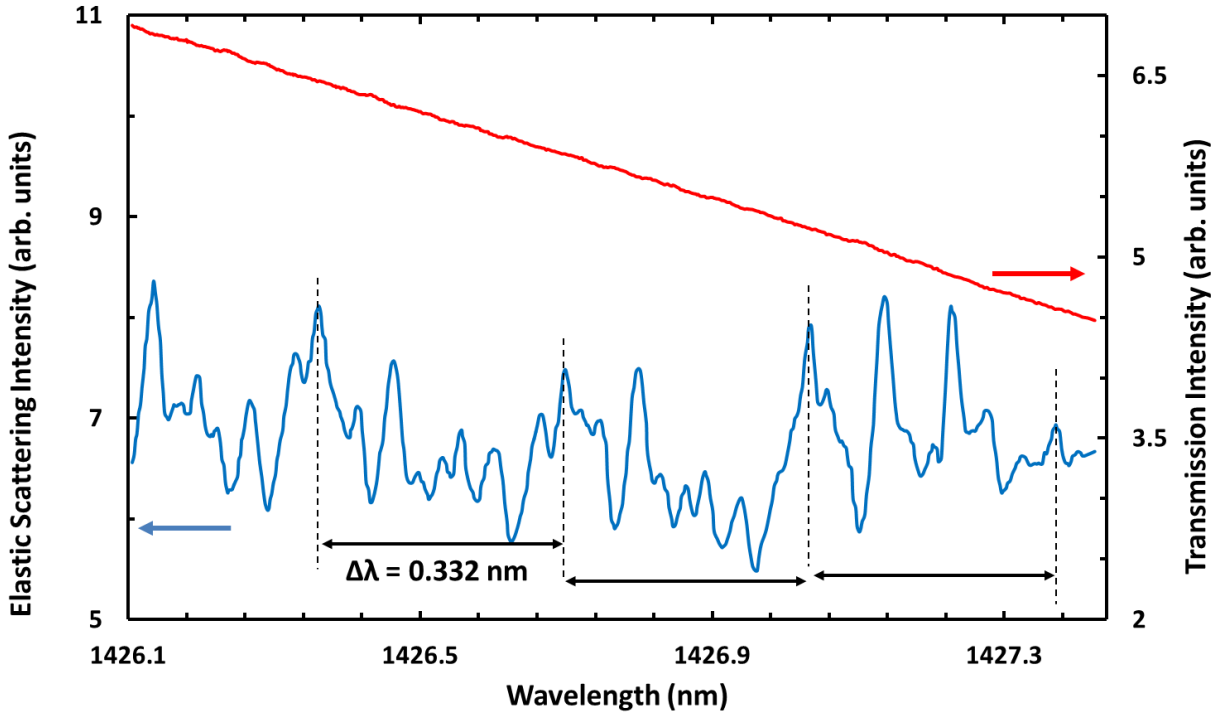

Fig. 5.5 TE polarized elastically scattering spectrum at 90° is shown in blue lower curve, and the transmission at 0° is shown in the red upper curve. The mode spacing of $\Delta\lambda_n$ = 0.332 nm.

Spacing between TE and TM polarizations for the resonant peaks with the same mode number, *n* is defined by [88]

$$\Delta\nu_{n,l}^{TE,TM} = \frac{c}{2\pi ma}\frac{\sqrt{m^2-1}}{m} \quad (4.1),$$

where $\Delta\nu_{n,l}^{TE,TM}$ is the spacing between the two transverse polarizations (TM and TE) in terms of frequency. The calculated value for $\Delta\nu_{n,l}^{TE,TM}$ is 45.6 GHz, that corresponds to $\Delta\lambda_{n,l}^{TE,TM}$ = 0.309 nm in terms

of wavelength. The spacing between the positions for the resonance peaks of two adjacent modes of TE and TM polarization is shown in Fig. 5.6. Measured $\Delta\lambda_{n,l}^{TE,TM}$ is 0.311 nm for the modes with identical mode numbers. The WGM resonance peaks with altered polarizations, that have the same mode number *n*, are at $\Delta\lambda_{n,l}^{TE}$ = 1426.48 nm and $\Delta\lambda_{n,l}^{TM}$ = 1426.79 nm for TM and TE, respectively. The experimental spacing between the two polarizations are in a respectable correlation with the results acquired by Eq. (4.1).

5.2.2 Size Parameter and Impact Parameter

Many of the conspicuous features of this elastic scattering geometry is defined by the interactions of a microsphere and an external Gaussian beam propagating at an impact parameter *b*, that is marginally greater than *a*. According to the conventional Lorenz-Mie theory, the size parameter *x* of the diamond microsphere is estimated by Eq. (2.14), where $N_{outside}$ is the external refractive index, which is in our case the refractive index of air.

At the resonance wavelength of 1426.29 nm, the size parameter is calculated as $x \approx 2200$. The number of modes around the microsphere are restricted by $x \leq n \leq mx$, where $m = 2.38$. The partial waves with *n* less than *x* should not be considered, since the excitation beam is placed beyond the edge of the microsphere, as justified by the localization principle [34] , thus the maximum mode excited in the microsphere is calculated as $mx \approx 5200$.

The localization principle associates a light beam having an impact parameter *b* with mode number *n* by [89]:

$$b = \left(n + \frac{1}{2} \right) \frac{a}{x} \tag{4.2}$$

which is restricted by $a \leq b \leq ma$ to satisfy the localization principle. Only the light rays possessing an impact parameter within the corresponding range are allowed to couple to the diamond microsphere to excite the WGMs. The maximum acceptable *b* is calculated as $b_{max} \approx 1.2$ mm away from the center of the microsphere. The diamond microsphere and the silica SMF OFHC are in contact to achieve light

coupling, with the core of the OFHC SMF 5 μm below the microsphere surface. Our value of $b \approx 505$ μm results in a mode number n = 2224.

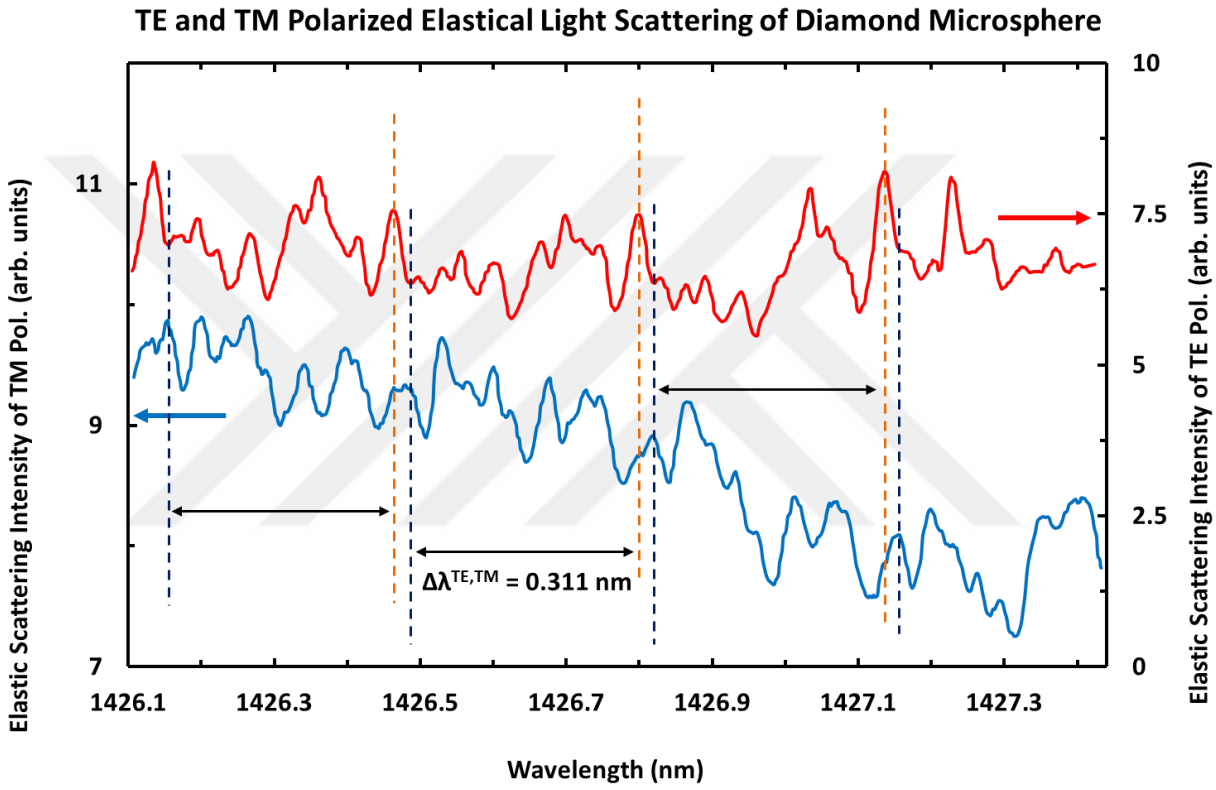

Fig. 5.6 TE (red) and TM (blue) polarizations along with the spacing of $\Delta\lambda_{n,l}^{TE,TM}$ = 0.311 nm between the two transverse polarizations.

5.2.3 Q-Factor

Stored light energy will eventually radiate out of the microresonator with a certain Q-factor depending on the physical condition of the microsphere. The measured Q-factor is determined by Eq. (2.7), where $\delta\lambda_{FWHM}$ is the full-width-at-half-maxima (FWHM) of one resonant peak at the central wavelength. The FWHM of the resonances are calculated by Lorentz shape fitting the resonant peak as shown in the Fig.

5.7. The TM polarized peak with the highest Q value is centered at 1426.63 nm with a FWHM of 32 pm, and calculated as 4.5×10^4. The rough calculation is performed with a homemade MATLAB code that is presented in APPENDIX A, along with the Q-factors of the resonances labeled on each peak for both TE and TM polarizations.

TE polarized 90° elastic scattering is recorded by placing the GP in perpendicular direction to the excitation OFHC. The Q-factor is calculated as 5.1×10^4 using Eq.(2.7), with $\delta\lambda_{FWHM} = 28$ pm at the central resonant wavelength $\lambda_n = 1426.80$ nm as shown in Fig. 5.8. There is only a slight difference between the measured TE and TM polarized Q-factors, and both of our measured Q-factors are comparable with previous works on circular diamond resonators [24, 25, 26, 27].

Our measurement setup, with a spectral resolution of 1 pm, puts an upper limit on the measurable Q-factor. However, independent from the measurement setup, we analyzed the potential limitations to the Q-factor. The Q-factor of a coupled spherical microcavity can theoretically be calculated by Eq. (2.37) and Eq. (2.42), where Q_{ext} is caused by the external coupling losses from the microsphere to the OFHC, Q_{rad} is due to intrinsic radiative losses, Q_{ss} is caused by scattering losses due to residual surface inhomogeneities, Q_{cont} is caused by surface contaminants, and Q_{mat} is due to material loss.

For our diamond microsphere with $2a/\lambda_n >> 15$, the intrinsic radiative losses (Q_{rad}^{-1}) can be neglected [6]. Similarly, for our experimental parameters, the loss caused by the surface contaminants (Q_{cont}^{-1}) is negligible [42]. Q_{ss} and Q_{mat} are defined as in Eq.(2.39) and Eq.(2.40), respectively, where $m = 2.38$ is the relative refractive index of diamond, and $\alpha < 1\ \mathrm{cm}^{-1}$ the intensity attenuation coefficient, depending on the nitrogen concentration inside the diamond lattice for type Ib diamond samples [65, 66], $D = 1$ mm the diameter of the microsphere, and σ and B the rms size and correlation length of the surface inhomogeneities, respectively. σ and B are both estimated as 20 nm on the surface of the diamond, thus the corresponding Q_{ss} is calculated to be on the order of 10^8 [27]. The estimated Q_{ss} significantly exceeds the measured Q-factor, and points the bulk optical losses as the source of optical energy dissipation at the microcavity. Q_{mat} is estimated to be on the order of 10^5 by using our experimental parameters. Higher nitrogen impurity levels inside the diamond lattice increase the infrared

absorption by Type Ib CVD diamonds, resulting in a smaller Q_{mat} value, thus limiting the achievable Q-factor.

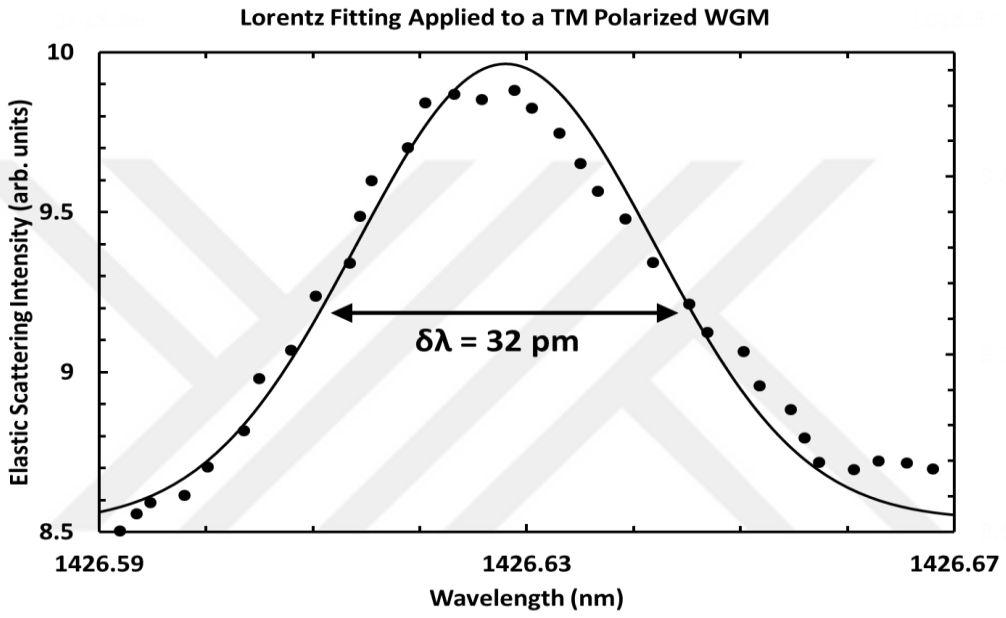

Fig. 5.7 Lorentz curve fitted TM polarized WGM centered at 1426.63 nm with a FWHM of 32 pm.

Compared to the other intrinsic contributions to the Q-factor, Q_{ext} is due to the external loading, and can be expressed by Eq.(2.43), where x is the size parameter as defined in Eq.(2.14), and t the incident light mode field coupling coefficient from the silica OFHC to the diamond microsphere. By using our experimental parameters, the Q-factor due to the coupling loss of the OFHC is calculated as $Q_{ext} \approx 1.38\times10^{4} / \left|t^{2}\right|$. $\left|t^{2}\right|$ is the fractional energy loss per circumnavigation round value and estimated to be << 1 for the OFHC mode – microsphere WGM coupling [47]. For our case of undercoupling to the microsphere, a Q-factor on the order of 10^8 can easily be achieved depending on the value of t, thus making the term Q_{ext}^{-1} in Eq. 5 negligible [49]. Therefore the primary limitation is caused

by Q_{mat} for the diamond microsphere resonator, which is further limited by the resolution of our measurement setup.

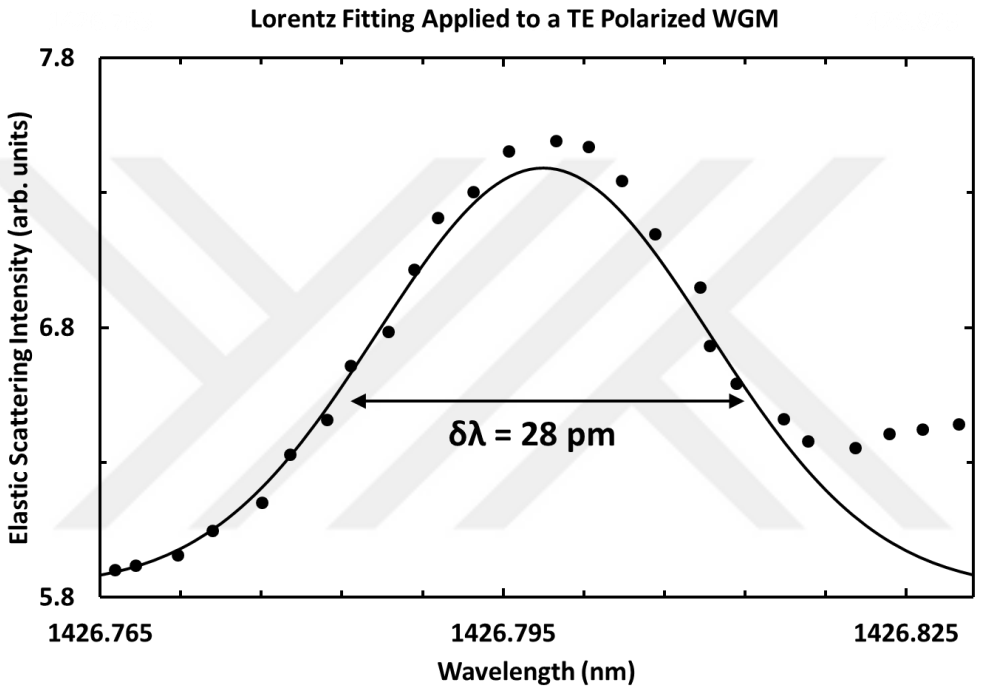

Fig. 5.8 Lorentz curve fitted TM polarized WGM centered at 1426.80 nm with a FWHM of 28 pm.

Chapter 6

CONCLUSION AND FUTURE WORK

In this thesis, Raman and photoluminescence (PL) spectroscopy of various diamond samples and elastic scattering from a diamond microsphere are studied. Influence of the nitrogen vacancy (NV) centers was discussed in terms of energy transitions and PL spectra. Similarly, a synthetic type Ib diamond microsphere is analyzed in terms of spectroscopy and morphology. The PL spectrum of the diamond microcavity yields the optical properties of the diamond, while the elastic scattering measurements give information about the morphology of the diamond. WGM resonances circumnavigate the diamond sphere, and the mode spacing, polarization, and Q-factor of these resonances are investigated.

In chapter 2 theory of optical resonators such as Fabry-Pérot resonators and spherical microcavities were discussed. The round trip, size parameter, mode spacing, Q-factor and coupling of spherical microresonators were analyzed, in the light of the Lorenz-Mie Theory. MDRs and WGMs are illustrated along with their possible energies, which can be stored in the optical microresonators with high Q-factors.

Chapter 3 summarizes the properties of the diamond carbon material in terms of physical and optical properties together with the energy transitions under photoexcitation. Physical qualities such as hardness, density and thermal expansion coefficient were discussed. Then, diamonds are categorized in to groups based on the nitrogen (N) impurities with their lattice. The refractive index and absorption coefficient of the diamond with respect to incident wavelength are analyzed as optical properties. The electronic energy transitions were presented for Raman scattering, NV^0 center PL and NV^- fluorescence.

In chapter 4, Raman and PL spectroscopy is performed with various diamond samples including the diamond microsphere. The measurement setup is presented for both spectroscopies. NV centers exhibit 575 nm or 637 nm ZPLs along with their corresponding phonon side bands (PSBs) depending on the charge state of the point defect, NV^0 and NV^-, respectively. A 572 nm inelastic Raman scattering is observed with 532 nm excitation laser due to the vibrational state of C-C bonds with sp^3 configuration, however sp^2 configuration yields inelastically scattered photons with 576 nm wavelength. It is possible to identify, the main impurities within the diamond lattice, and confirm the C-C bonds with spectroscopic techniques.

In chapter 5, WGM resonances of a 1 mm monocrystalline diamond microsphere coupled with an OFHC were observed in the near-IR. The mode spacing of the resonances was measured as 0.332 nm, and the Q-factor on the order of 10^4 was observed, for both TE and TM polarizations. The calculated value of the mode spacing is 0.340 nm, and the expected shift of the mode in terms of wavelength between TE and TM is 0.247 nm, where the measured difference is 0.268 nm. In addition to the limitation due to the resolution of the measurement setup, the bulk optical scattering (Q_{mat}) losses were identified as the limiting mechanism on the Q-factor. With an improvement of the experimental spectral resolution, it would be possible to measure higher Q-factor WGMs.

Diamond microresonators with their high Q-factor WGMs can be used as stable optical frequency comb generators or lasing microcavities by exploiting the nitrogen vacancy centers within the lattice of the diamond. Very recently, stimulated emission from the NV centers was observed of Type Ib diamond samples [90]. If the stimulated emission of the NV centers can be realized at the diamond microsphere, then it is possible to observe the lasing of NV^0 or NV^- center PL, which has not been observed before. The Q-factor of the diamond microresonator is on the order of 10^4, thus can give rise to lasing action of a PL at 575 nm or 637 nm, and/or of Raman scattering at 572 nm with a 532 nm excitation laser. Previously, lasing action of Raman scattering by a diamond ring resonator is achieved [19]. However, this phenomenon was observed in the near-IR regime, thus no lasing action was observed in the visible regime before from a diamond spherical cavity. Therefore, it is possible to exploit the high Q-factor of the diamond microsphere resonator to establish a diamond laser in the visible spectrum.

APPENDIX A

A.1. MATLAB Script for Mode Spacing, Size Parameter and TE vs. TM Mode Spacing Difference Calculation

```
%% Mode Spacing, Size Parameter, TE and TM Spacing Calculator.
% This code calculates the mode spacing in terms of frequency and
% wavelength,
% calculates the size parameter and
% calculates the frequency shift between TE and TM modes in GHz.
% You will be asked to write the resonance wavelength in nm,
% radius of the microsphere in um, and
% relative refractive index.
% Results will be printed on Matlab via fprintf.

%%

clear all
clc
lmd=input('Central Wavelength in nm:   ');
a=input('Radius in um:     ');
a1=a*10^-6;
lmd1=lmd*10^-9;
m=input('Relative Refractive index at the desired wavelength:  ');
b=input('Impact Parameter in um:     ');
c= 3*10^8;
z=sqrt((m^2)-1)/m;


z=sqrt((m^2)-1)/m;
FreqFSR=(c/(2*pi*a1))*((atan(sqrt((m^2)-1)))/sqrt((m^2)-1));
TEdifTM=FreqFSR*z*10^-9;

Freq1=FreqFSR*10^-9;
WavFSR= ((lmd1^2)*atan(sqrt((m^2)-1)))/((2*pi*a1)*sqrt((m^2)-1));

Wav1=WavFSR*10^9;
x=(2*pi*a1)/(lmd1);
```

```
n=(((b*x)/a)-(1/2));

PolDifWav=Wav1*z;

fprintf('Size Parameter: %f  \n',x)
fprintf('Mode Spacing in Frequency: %f GHz  \n',Freq1)
fprintf('Mode Spacing in Wavelength: %f nm \n',Wav1)
fprintf('Frequency Spacing Between TE and TM Modes:  %f GHz \n',TEdifTM)
fprintf('Mode Spacing Between TE and TM Modes:  %f nm \n',PolDifWav)
fprintf('Mode Number: %f  \n',n)
```

A.2. MATLAB Script for Q-factor Calculation

```
%% Q –Factor Calculator

% This code reads data from a defined Excel File in a defined directory.
% Code selects x-axis data from B column y-axis data from E column. (can be changed)
% Code flips the data if its not in an ascending manner for x-axis.
% Code locates the local maxima and local minima of the spectra.
% YOU NEED TO DEFINE A CONDITION TO GET RID SMALL PEAKS (Check code:
pkmax-pkmin)
% Code yields the FWHM, Q-factor, Central Wavelength, FWHM x1 and x2 as text for
each peak.
% Code displays the graph with Q-factors written on each peak.
% Code gives the maximum possible Q-factor at the end.

%%

clc
clear all

fname='C:\Users\Mert Bayer\Desktop\Diamond Resonance_TM_final_v1.xls'; %Enter
File Name
x=xlsread(fname,'data','B:B'); %Define the Sheet name and Column for x-axis in the
Excel File
y=xlsread(fname,'data','E:E'); %Define the Sheet name and Column for y-axis in the
Excel File
plot(x,y,'.')          %Plotting Data points
```

```
hold on

dumi=y;
wis=1;          %Sensitivity of the filtering for best curve fitting
a=1;
b = (1/wis)*ones(1,wis);
yfilt=filter(b,a,y);        %filtering the data
y=yfilt;

if x(1)>x(2)        % x-values should be in increasing order, this line flips if x-values are
descending
x=flip(x);
y=flip(y);
end
[pkmax,locmax]=findpeaks(y,x); % Locates the local maxima
yi=-1*y;
[pkmin,locmin]=findpeaks(yi,x); % Locates the local minima
pkmin=abs(pkmin);
Q1=[];
Q2=[];

findpeaks(y,x)

for i=1:length(pkmax)-2         %loop that calculates the Q factor.
    HM=(((pkmin(i)+pkmin(i+1))/2)+pkmax(i))/2;
    lim1=find(x==locmin(i+1));
    lim2=find(x==locmin(i));
        xnew=x(lim2:lim1);
        ynew=y(lim2:lim1);
        xpos1=find(HM>=ynew);
        a1=xnew(xpos1(end));
        a2=xnew(xpos1(1));
        b1=ynew(xpos1(end));
        b2=ynew(xpos1(1));
        FWHM=a1-a2;    % FWHM calculation
        Q=locmax(i)/FWHM;
        Q2=[Q2 Q];

            if Q~=Inf && pkmax(i)-pkmin(i)>0.2  %defined conditions to limit the possible
Q-factors to be shown on the graph.
```

```
        Q1=[Q1 Q];                                  % i.e. if the peak size is smaller than 0.2
don't show on the graph.
            h=text(locmax(i),pkmax(i)+0.1,num2str(Q), 'Fontsize',14);
        set(h,'rotation', 90);
           end

fprintf('FWHM of the given series is: %f nm. \n',FWHM)
fprintf('Q factor of the given series is: %f. \n',Q)
fprintf('Central Wavelength of the given series is: %f nm. \n',locmax(i))
fprintf('Between %f nm and %f nm. \n',locmin(i),locmin(i+1))
fprintf('HALF: %f, y1: %f  and y2: %f au. \n',HM,b1,b2)
fprintf('\n')
end
        plc=find(max(Q1)==Q2);
       locdum=locmax(plc);
qmax=max(Q1);
fprintf('MAX Q factor of the given series is: %f and centered at %f.\n',qmax,locdum)
hold on
plot(locmin,pkmin,'red o')
ylim([min(y)-0.25 max(y)+0.25]);
xlabel('Wavelength (nm)','Fontsize',24)
ylabel('Intensity (arb. units)','Fontsize',24)
title('Q-factors of TE Polarized Resonances','Fontsize',24)
```

A.3. TM Polarized 90º Elastically Scattered WGM Q-factors

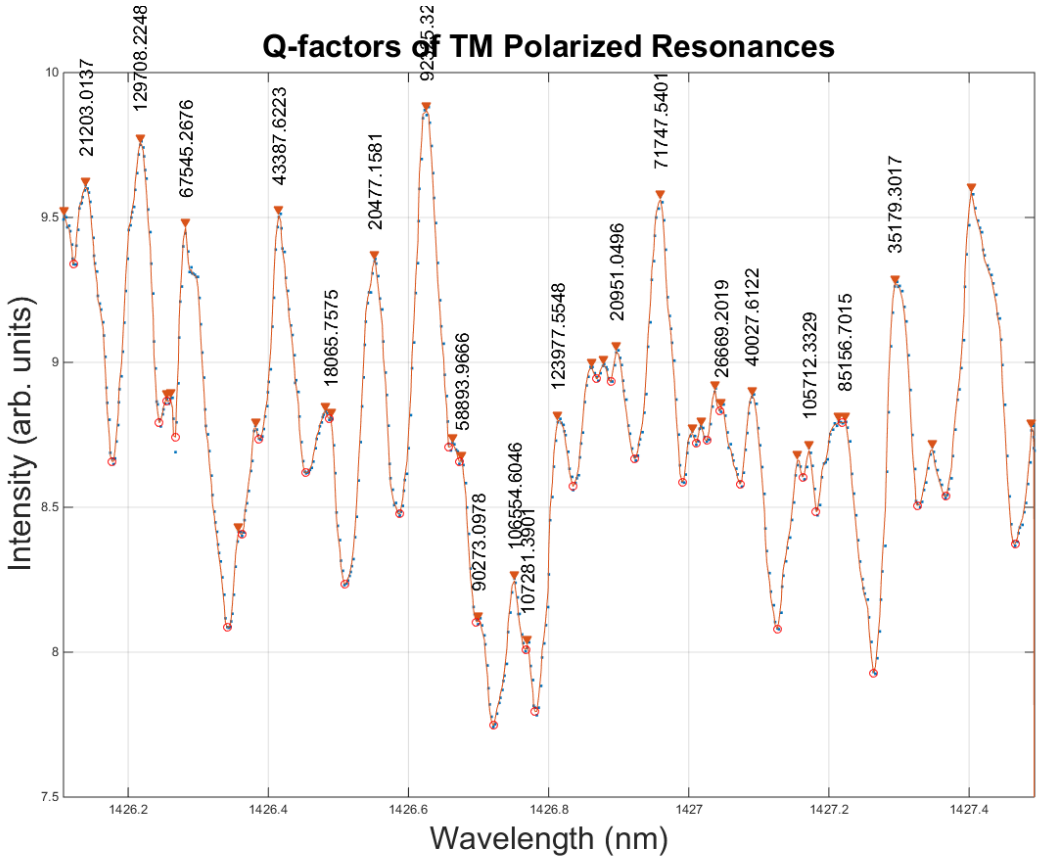

Fig. A.1. Calculated Q-factors of TM polarized WGMs by the MATLAB script.

A.4. TE Polarized 90º Elastically Scattered WGM Q-factors

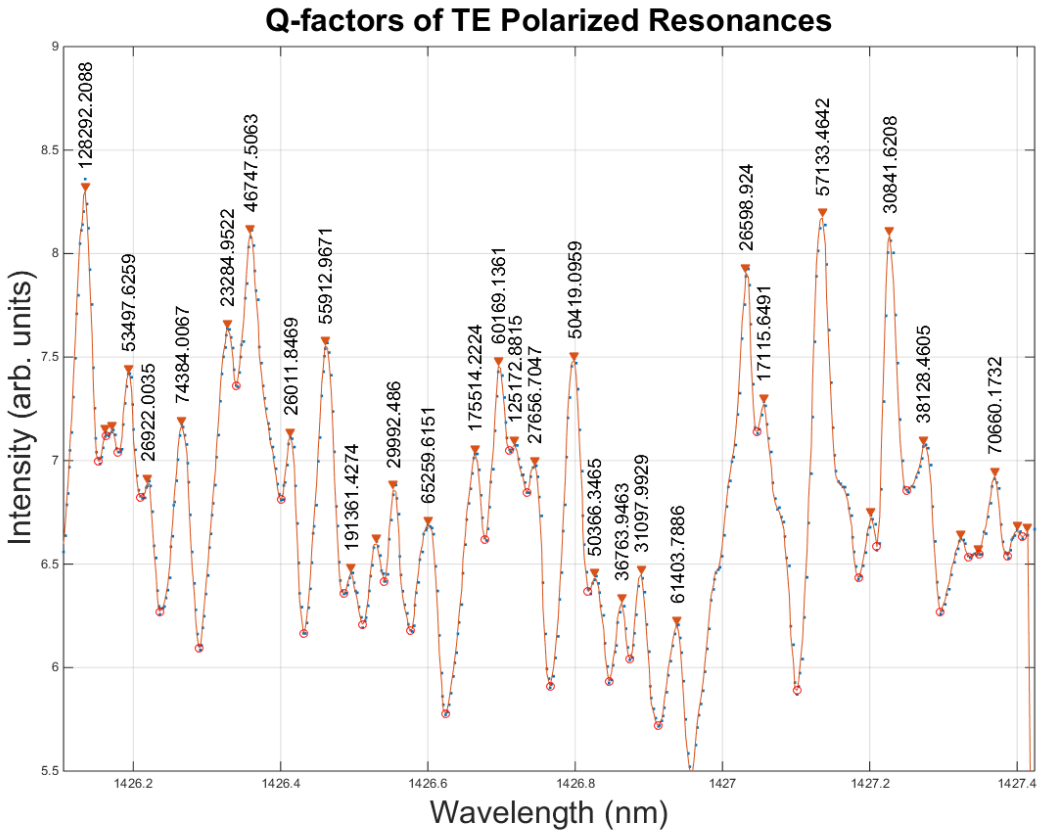

Fig. A.2. Calculated Q-factors of TE polarized WGMs by the MATLAB script.

VITA

Mustafa Mert Bayer completed his high school studies in VKV Koç Özel Lisesi, Istanbul Turkey in 2010. He received his Bachelor of Science degrees in Physics, and Electric and Electronics Engineering from VKV Koç University in Istanbul, Turkey in 2015, along with an Optics and Electromagnetism Track certificate. He then joined the Master of Science. program in Optoelectronics and Photonics Engineering at VKV Koç University in Istanbul, Turkey in 2015, as a teaching and research assistant during which, he worked on Diamond Photonics with professor Ali Serpengüzel at VKV Koç University Microphotonics Research Laboratory. As of Fall 2017, he plans to continue his Doctor of Philosophy in Science at University of California (UC) Irvine working with professor Özdal Boyraz at the Advanced Photonic Devices and Systems Laboratory at UC Irvine, California, USA.

List of Publications and Conferences

1. O. M. Öztürk, M. M. Bayer, M. S. Anwar, M. Zakwan and A. Serpengüzel, "Spectroscopy of a Nd: YVO_4 diode pumped solid state laser," Microwave and Optical Technology Letters 59, 1636–1639 (2017).
2. M. M. Bayer, H.O. Çirkinoğlu and A. Serpengüzel, "Whispering Gallery Modes of a Diamond Microsphere." (Under Review at IEEE Photonic Technology Letters)
3. M. H. Humayun, S. S. S. Bukhari, M. Zakwan, M. M. Bayer, U. S. Gökay, A. Serpengüzel, E. Omura and J. Nakata, "Enhancement of the Spherical Silicon Photocell Response by Elastic and Inelastic Scattering with Immersion in Amorphous and Crystalline Liquids." (Under Review at Applied Optics)
4. H.O. Çirkinoğlu, M. M. Bayer, A. Serpengüzel, B. Sotillo, V. Bharadwaj, R. Ramponi and S. M. Eaton, "Femtosecond Laser Written Shallow Diamond Waveguide Excitation of Whispering Gallery Modes in a Silicon Microsphere" (In Progress)
5. S. Sultan Shah Bukhari, M. R. Chaudhry, M. M. Bayer, and A. Serpengüzel, "Elastic Scattering from a Sapphire Microsphere in the THz Region," in *Frontiers in Optics 2016*, (Optical Society of America) *Rochester, New York, USA* p. JTh2A.180.
6. M. Zakwan, M. M. Bayer, M. S. Anwar, U. S. Gökay, and A. Serpengüzel, "Mid-infrared elastic scattering from germanium microspheres," in *International Conference on Transparent Optical Networks (ICTON) 2016, Trento, Italy*.

BIBLIOGRAPHY

[1] J. Ward and O. Benson, "WGM microresonators: sensing, lasing and fundamental optics with microspheres," Laser & Photonics Reviews **5**, 553–570 (2011).

[2] R. E. Benner, P. W. Barber, J. F. Owen, and R. K. Chang, "Observation of Structure Resonances in the Fluorescence Spectra from Microspheres," Physical Review Letters **44**, 475–478 (1980).

[3] J. P. Laine, C. Tapalian, B. Little, and H. Haus, "Acceleration sensor based on high-Q optical microsphere resonator and pedestal antiresonant reflecting waveguide coupler," Sensors and Actuators A: Physical **93**, 1–7 (2001).

[4] A. B. Matsko and V. S. Ilchenko, "Optical resonators with whispering gallery modes I: basics," IEEE Journal of Selected Topics in Quantum Electronics **12**, 3 (2006).

[5] X. Peng, F. Song, S. Jiang, N. Peyghambarian, M. Kuwata-Gonokami, and L. Xu, "Fiber-taper-coupled L-band Er3+-doped tellurite glass microsphere laser," Applied Physics Letters **82**, 1497–1499 (2003).

[6] V. S. Ilchenko, M. Gorodetsky, and S. Vyatchanin, "Coupling and tunability of optical whispering-gallery modes: a basis for coordinate meter," Optics Communications **107**, 41–48 (1994).

[7] J. C. Knight, N. Dubreuil, V. Sandoghdar, J. Hare, V. Lefèvre-Seguin, J. M. Raimond, and S. Haroche, "Mapping whispering-gallery modes in microspheres with a near-fieldprobe," Optics Letters **20**, 1515–1517 (1995).

[8] R. K. Chang and P. W. Barber, *Optical Effects Associated with Small Particles* (World Scientific, 1988), Vol. 1.

[9] A. A. Savchenkov, V. S. Ilchenko, A. B. Matsko, and L. Maleki, "Kilohertz optical resonances in dielectric crystal cavities," Physical Review A **70**, 51804 (2004).

[10] K. J. Vahala, "Optical microcavities," Nature **424**, 839–846 (2003).

[11] N. Mounet and N. Marzari, "First-principles determination of the structural, vibrational and thermodynamic properties of diamond, graphite, and derivatives," Physical Review B **71**, 205214 (2005).

[12] J. Walker, "Optical absorption and luminescence in diamond," Reports on Progress in Physics **42**, 1605 (1979).

[13] J. P. M. Feve, K. E. Shortoff, M. J. Bohn, and J. K. Brasseur, "High average power diamond Raman laser," Optics Express **19**, 913–922 (2011).

[14] X. H. Wu, Z. N. Chen, and N. Yang, "Optimization of planar diamond antenna for single-band and multiband UWB wireless communications," Microwave and Optical Technology Letters **42**, 451–455 (2004).

[15] S. Prawer and I. Aharonovich, Quantum Information Processing with Diamond: Principles and Applications (Elsevier, 2014).

[16] I. Taher, M. Aslam, M. Tamor, T. Potter, and R. Elder, "Piezoresistive microsensors using p-type CVD diamond films," Sensors and Actuators A: Physical **45**, 35–43 (1994).

[17] E. Kohn and A. Denisenko, "Concepts for diamond electronics," Thin Solid Films **515**, 4333–4339 (2007).

[18] I. Aharonovich, A. D. Greentree, and S. Prawer, "Diamond photonics," Nature Photonics **5**, 397–405 (2011).

[19] P. Latawiec, V. Venkataraman, M. J. Burek, B. J. M. Hausmann, I. Bulu, and M. Lončar, "On-chip diamond Raman laser," Optica **2**, 924–928 (2015).

[20] M. Cai, O. Painter, K. J. Vahala, and P. C. Sercel, "Fiber-coupled microsphere laser," Optics Letters **25**, 1430–1432 (2000).

[21] A. Serpengüzel, A. Kurt, and U. K. Ayaz, "Silicon microspheres for electronic and photonic integration," Photonics and Nanostructures-Fundamentals and Applications **6**, 179–182 (2008).

[22] P. Wang, T. Lee, M. Ding, A. Dhar, T. Hawkins, P. Foy, Y. Semenova, Q. Wu, J. Sahu, and G. Farrell, "Germanium microsphere high-Q resonator," Optics Letters **37**, 728–730 (2012).

[23] K. E. Spear and J. P. Dismukes, *Synthetic Diamond: Emerging CVD Science and Technology* (John Wiley & Sons, 1994), Vol. 25.

[24] B. J. M. Hausmann, I. B. Bulu, P. B. Deotare, M. McCutcheon, V. Venkataraman, M. L. Markham, D. J. Twitchen, and M. Lončar, "Integrated High-Quality Factor Optical Resonators in Diamond," Nano Letters **13**, 1898–1902 (2013).

[25] B. J. M. Hausmann, I. Bulu, V. Venkataraman, P. Deotare, and M. Loncar, "Diamond nonlinear photonics," Nature Photonics **8**, 369 (2014).

[26] A. Faraon, P. E. Barclay, C. Santori, K.-M. C. Fu, and R. G. Beausoleil, "Resonant enhancement of the zero-phonon emission from a colour centre in a diamond cavity," Nature Photonics **5**, 301–305 (2011).

[27] V. S. Ilchenko, A. M. Bennett, P. Santini, A. A. Savchenkov, A. B. Matsko, and L. Maleki, "Whispering gallery mode diamond resonator," Optics Letters **38**, 4320–4323 (2013).

[28] K. Vahala, *Optical Microcavities* (World Scientific, 2004), Vol. 5.

[29] U. Keller, D. A. B. Miller, G. D. Boyd, T. H. Chiu, J. F. Ferguson, and M. T. Asom, "Solid-state low-loss intracavity saturable absorber for Nd:YLF lasers: an antiresonant semiconductor Fabry–Perot saturable absorber," Optics Letters **17**, 505–507 (1992).

[30] S. B. Papp, K. Beha, P. Del'Haye, F. Quinlan, H. Lee, K. J. Vahala, and S. A. Diddams, "Microresonator frequency comb optical clock," Optica **1**, 10–14 (2014).

[31] M. Pöllinger, D. O'Shea, F. Warken, and A. Rauschenbeutel, "Ultrahigh-Q Tunable Whispering-Gallery-Mode Microresonator," Physical Review Letters **103**, 53901 (2009).

[32] C. F. Bohren and D. R. Huffman, *Absorption and Scattering of Light by Small Particles* (John Wiley & Sons, 2008), pp. 100.

[33] G. Righini, Y. Dumeige, P. Féron, M. Ferrari, G. Nunzi Conti, D. Ristic, and S. Soria, "Whispering gallery mode microresonators: fundamentals and applications," Rivista del Nuovo Cimento **34**, 435–488 (2011).

[34] H. C. van de Hulst, *Light Scattering by Small Particles* (Dover, 1981).

[35] G. Mie, "Beiträge zur Optik trüber Medien, speziell kolloidaler Metallösungen," Annalen der Physik **330**, 377–445 (1908).

[36] J. A. Lock and G. Gouesbet, "Generalized Lorenz–Mie theory and applications," Journal of Quantitative Spectroscopy and Radiative Transfer **110**, 800–807 (2009).

[37] J. A. Lock, "Improved Gaussian beam-scattering algorithm," Applied Optics **34**, 559–570 (1995).

[38] P. Chýlek, "Partial-wave resonances and the ripple structure in the Mie normalized extinction cross section," Journal of Optical Society of America A **66**, 285–287 (1976).

[39] P. Chýlek, "Resonance structure of Mie scattering: distance between resonances," Journal of Optical Society of America A **7**, 1609–1613 (1990).

[40] P. Chýlek, J. T. Kiehl, and M. K. W. Ko, "Narrow resonance structure in the Mie scattering characteristics," Applied Optics **17**, 3019–3021 (1978).

[41] D. Kajfez and P. Guillon, *Dielectric Resonators* (Noble Publishing Corp, 1998).

[42] M. L. Gorodetsky, A. A. Savchenkov, and V. S. Ilchenko, "Ultimate Q of optical microsphere resonators," Optics Letters **21**, 453–455 (1996).

[43] A. Chiasera, Y. Dumeige, P. Feron, M. Ferrari, Y. Jestin, G. Nunzi Conti, S. Pelli, S. Soria, and G. C. Righini, "Spherical whispering-gallery-mode microresonators," Laser & Photonics Reviews **4**, 457–482 (2010).

[44] K. Guenther and P. Wierer, "Surface roughness assessment of ultrasmooth laser mirrors and substrates," in (International Society for Optics and Photonics, 1983), pp. 266–279.

[45] D. Pinnow, T. Rich, F. Ostermayer Jr, and M. DiDomenico Jr, "Fundamental optical attenuation limits in the liquid and glassy state with application to fiber optical waveguide materials," Applied Physics Letters **22**, 527–529 (1973).

[46] I. L. Fabelinskii, *Molecular Scattering of Light* (Springer Science & Business Media, 2012).

[47] G. Griffel, J. Connolly, N. Morris, S. Arnold, D. Taskent, and A. Serpengüzel, "Morphology-dependent resonances of a microsphere–optical fiber system," Optics Letters **21**, 695–697 (1996).

[48] S. Spillane, T. Kippenberg, O. Painter, and K. Vahala, "Ideality in a fiber-taper-coupled microresonator system for application to cavity quantum electrodynamics," Physical Review Letters **91**, 43902 (2003).

[49] M. L. Gorodetsky and V. S. Ilchenko, "Optical microsphere resonators: optimal coupling to high-Q whispering-gallery modes," Journal of Optical Society of America B **16**, 147–154 (1999).

[50] M. Scarselli, P. Castrucci, and M. De Crescenzi, "Electronic and optoelectronic nano-devices based on carbon nanotubes," Journal of Physics: Condensed Matter **24**, 313202 (2012).

[51] H. Sumiya, N. Toda, and S. Satoh, "Mechanical properties of synthetic type IIa diamond crystal," Diamond and Related Materials **6**, 1841–1846 (1997).

[52] T. Anthony, W. Banholzer, J. F. Fleischer, L. Wei, P. Kuo, R. Thomas, and R. Pryor, "Thermal diffusivity of isotopically enriched C 12 diamond," Physical Review B **42**, 1104 (1990).

[53] Azo Materials, "Diamond (C) - Properties, Applications," http://www.azom.com/article.aspx?ArticleID=262.

[54] M. Murakawa and S. Takeuchi, "Mechanical applications of thin and thick diamond films," Surface and Coatings Technology **49**, 359–364 (1991).

[55] M. W. Doherty, N. B. Manson, P. Delaney, F. Jelezko, J. Wrachtrup, and L. C. L. Hollenberg, "The nitrogen-vacancy colour centre in diamond," Physics Reports **528**, 1–45 (2013).

[56] L. Childress, R. Walsworth, and M. Lukin, "Atom-like crystal defects," Physics Today **67**, 38 (2014).

[57] A. T. Collins, "The characterisation of point defects in diamond by luminescence spectroscopy," Diamond and Related Materials **1**, 457–469 (1992).

[58] A. Grill, "Electrical and optical properties of diamond-like carbon," Thin Solid Films **355**, 189–193 (1999).

[59] D. F. Edwards and E. Ochoa, "Infrared refractive index of diamond," Journal of Optical Society of America A **71**, 607–608 (1981).

[60] F. Peter, "Über Brechungsindizes und Absorptionskonstanten des Diamanten zwischen 644 und 226 mμ," Zeitschrift für Physik A Hadrons and Nuclei **15**, 358–368 (1923).

[61] H. Philipp and E. Taft, "Optical properties of diamond in the vacuum ultraviolet," Physical Review **127**, 159 (1962).

[62] H. R. Phillip and E. A. Taft, "Kramers-Kronig Analysis of Reflectance Data for Diamond," Physical Review **136**, A1445–A1448 (1964).

[63] A. M. Zaitsev, *Optical Properties of Diamond: A Data Handbook* (Springer Science & Business Media, 2013).

[64] R. P. Mildren, "Intrinsic optical properties of diamond," Optical Engineering of Diamond 1–34 (2013).

[65] R. U. A. Khan, P. M. Martineau, B. Cann, M. Newton, and D. Twitchen, "Charge transfer effects, thermo and photochromism in single crystal CVD synthetic diamond," Journal of Physics: Condensed Matter **21**, 364214 (2009).

[66] Q. Liang, C. Yan, Y. Meng, J. Lai, S. Krasnicki, H. Mao, and R. J. Hemley, "Recent advances in high-growth rate single-crystal CVD diamond," Diamond and Related Materials **18**, 698–703 (2009).

[67] W. H. Weber and R. Merlin, *Raman Scattering in Materials Science* (Springer Science & Business Media, 2013), Vol. 42.

[68] D. A. Long and D. Long, *Raman Spectroscopy* (McGraw-Hill New York, 1977).

[69] S. A. Solin and A. K. Ramdas, "Raman Spectrum of Diamond," Physical Review B **1**, 1687–1698 (1970).

[70] E. D. Obraztsova, K. Korotushenko, S. Pimenov, V. Ralchenko, A. Smolin, V. Konov, and E. Loubnin, "Raman and photoluminescence investigations of nanograined diamond films," Nanostructured Materials **6**, 827–830 (1995).

[71] N. Aslam, G. Waldherr, P. Neumann, F. Jelezko, and J. Wrachtrup, "Photo-induced ionization dynamics of the nitrogen vacancy defect in diamond investigated by single-shot charge state detection," New Journal of Physics **15**, 13064 (2013).

[72] S. Karaveli, O. Gaathon, A. Wolcott, R. Sakakibara, O. A. Shemesh, D. S. Peterka, E. S. Boyden, J. S. Owen, R. Yuste, and D. Englund, "Modulation of nitrogen vacancy charge state and fluorescence in nanodiamonds using electrochemical potential," Proceedings of the National Academy of Sciences **113**, 3938–3943 (2016).

[73] J. Wolters, A. W. Schell, G. Kewes, N. Nüsse, M. Schoengen, H. Döscher, T. Hannappel, B. Löchel, M. Barth, and O. Benson, "Enhancement of the zero phonon line emission from a single nitrogen vacancy center in a nanodiamond via coupling to a photonic crystal cavity," Applied Physics Letters **97**, 141108 (2010).

[74] F. Waldermann, P. Olivero, J. Nunn, K. Surmacz, Z. Wang, D. Jaksch, R. Taylor, I. Walmsley, M. Draganski, and P. Reichart, "Creating diamond color centers for quantum optical applications," Diamond and Related Materials **16**, 1887–1895 (2007).

[75] K. Beha, A. Batalov, N. B. Manson, R. Bratschitsch, and A. Leitenstorfer, "Optimum photoluminescence excitation and recharging cycle of single nitrogen-vacancy centers in ultrapure diamond," Physical Review Letters **109**, 97404 (2012).

[76] S. Castelletto, X. Li, and M. Gu, "Frontiers in diffraction unlimited optical methods for spin manipulation, magnetic field sensing and imaging using diamond nitrogen vacancy defects," Nanophotonics **1**, 139–153 (2012).

[77] N. Bar-Gill, L. M. Pham, A. Jarmola, D. Budker, and R. L. Walsworth, "Solid-state electronic spin coherence time approaching one second," Nature Communications **4**, 1743 (2013).

[78] Y. Liu, G. Chen, Y. Rong, L. P. McGuinness, F. Jelezko, S. Tamura, T. Tanii, T. Teraji, S. Onoda, and T. Ohshima, "Fluorescence polarization switching from a single silicon vacancy colour centre in diamond," Scientific Reports **5**, (2015).

[79] R. E. Ledley III, "Electronic digital micrometer," (1978).

[80] Dutch Diamond Technologies, "Grades and Shapes. DD-Technologies | Dutch Diamond Technologies." http://www.dd-technologies.com/grades-and-shapes/.

[81] Renishaw Corp., "Renishaw: Custom Raman solutions," http://www.renishaw.com/en/custom-raman-solutions--6881.

[82] A. Karczemska, M. Szurgot, M. Kozanecki, M. Szynkowska, V. Ralchenko, V. Danilenko, P. Louda, and S. Mitura, "Extraterrestrial, terrestrial and laboratory diamonds—Differences and similarities," Diamond and Related Materials **17**, 1179–1185 (2008).

[83] H. Masuda, T. Yanagishita, K. Yasui, K. Nishio, I. Yagi, T. N. Rao, and A. Fujishima, "Synthesis of well-aligned diamond nanocylinders," Advanced Materials **13**, 247–249 (2001).

[84] S. C. Eaton-Magaña and K. S. Moe, "Temperature effects on radiation stains in natural diamonds," Diamond and Related Materials **64**, 130–142 (2016).

[85] Changchun New Industries Optoelectronics Tech. Co. Ltd. "CNI SLM single longitudinal mode 532 nm laser," http://www.cnilaser.com/single_frequency_laser532.htm.

[86] Stanford Research Systems,Inc, "Lock In Amplifier - SR830 and SR810," http://www.thinksrs.com/products/SR810830.htm.

[87] K. Beha, H. Fedder, M. Wolfer, M. C. Becker, P. Siyushev, M. Jamali, A. Batalov, C. Hinz, J. Hees, and L. Kirste, "Diamond nanophotonics," Beilstein Journal of Nanotechnology **3**, 895–908 (2012).

[88] V. Datsyuk, "Some characteristics of resonant electromagnetic modes in a dielectric sphere," Applied Physics B **54**, 184–187 (1992).

[89] A. Serpengüzel, S. Arnold, G. Griffel, and J. A. Lock, "Enhanced coupling to microsphere resonances with optical fibers," Journal of Optical Society of America B **14**, 790–795 (1997).

[90] J. Jeske, D. W. Lau, X. Vidal, L. P. McGuinness, P. Reineck, B. C. Johnson, M. W. Doherty, J. C. McCallum, S. Onoda, and F. Jelezko, "Stimulated emission from nitrogen-vacancy centres in diamond," Nature Communications **8**, 14000 (2017).